*J. Fluid Mech.* (1994), *vol.* 271, *pp.* 235–265



# The influence of thermal noise on the onset of travelling-wave convection in binary fluid mixtures: an experimental investigation

By WOLFGANG SCHÖPF† AND INGO REHBERG
Physikalisches Institut der Universität Bayreuth, 95440 Bayreuth, Germany

(Received 7 May 1993 and in revised form 24 January 1994)

When dealing with systems showing a Hopf bifurcation as the first instability from a conductive state leading to travelling waves, the distinction between convective and absolute instability becomes significant. The convectively unstable regime is characterized by the fact that a homogeneous disturbance may have a positive growth rate, while a single localized perturbation cannot trigger the onset of nonlinear convection. In this paper the convective instability occurring in binary fluid mixtures for a negative separation ratio is utilized for amplifying intrinsic thermal fluctuations, which in this way become accessible to quantitative measurements. The experiments are performed in a quasi-one-dimensional convection channel which, by means of subcritical ramps, effectively prevents the reflection of the travelling waves from the sidewalls. Thus, that range of the convective instability within which linear waves can be observed is strongly enhanced. The temperature variations involved in the observed travelling-wave states are quantified by using the shadowgraph method. By resonantly stimulating the system with its linear Hopf frequency, the reflection ability and some coefficients of the amplitude equation appropriate for describing the convection features near onset can be determined. Without stimulation, travelling-wave states of very small amplitudes showing an erratic spatio-temporal behaviour occur spontaneously inside the convectively unstable regime. The temporal correlation function calculated from the measured light intensity caused by these states is compared with a theoretical expression obtained from a Ginzburg–Landau equation containing a noise term. A very good agreement is found for the amplitude if thermal noise is assumed to be the reason for these fluctuating convection rolls, thus supporting the idea that the response of the system to thermal fluctuations is observed.

## 1. Introduction

In many nonlinear dissipative systems which are driven out of equilibrium by being subjected to an external stress $R$, a pattern-forming instability can arise when the driving force exceeds a critical value $R_c$. In fact much of the effort expended in investigating chaos and turbulence in fluids has recently been devoted to the understanding of the common features of such bifurcations from a temporally and spatially uniform basic configuration to a state of lower symmetry showing a characteristic spatial and possibly temporal variation (for numerous examples see the conference

† Present address: Centre for Water Research, University of Western Australia, Nedlands WA 6009, Australia

proceedings edited by Swinney & Gollub 1981; Wesfreid *et al.* 1988; Coullet & Huerre 1990; Busse & Kramer 1990). Systems undergoing such behaviour are widespread in physics, chemistry and biology. Within fluid dynamics, the best-known examples of pattern-forming instabilities are probably the thermally driven Rayleigh–Bénard system (Bénard 1900; Rayleigh 1916; Chandrasekhar 1961) and rotating Taylor–Couette flow (Taylor 1923; Chandrasekhar 1961; DiPrima & Swinney 1981). In recent years the study of electrohydrodynamic convection in a nematic liquid crystal has become increasingly paradigmatic (for an overview see e.g. Bodenschatz, Zimmermann & Kramer 1988; Rehberg *et al.* 1989). These hydrodynamic systems share the advantage that they are easily controllable from an experimental point of view and that the fundamental equations describing their behaviour are usually well-known.

Another example which has attracted much attention during the last 20 years is the Rayleigh–Bénard convection in binary fluids (for an overview see e.g. Gershuni & Zhukhovitskii 1976; Platten & Legros 1984). Here a mixture of two miscible fluids like water–alcohol or $^3$He–$^4$He rather than a pure fluid is used as the working medium. The two-component nature of the mixture gives rise to the occurrence of the Soret effect, which behaves as a second control parameter besides the Rayleigh number $R$. This new parameter, the so-called separation ratio $\psi$, measures the stabilizing ($\psi < 0$) or destabilizing ($\psi > 0$) effect of the concentration gradient. In this system, convection can happen not only in the form of a stationary roll pattern as in the normal Rayleigh–Bénard experiment. Depending on $\psi$ the possibility of a Hopf bifurcation also exists, leading to time-periodic states which in the simplest case can manifest themselves as travelling or standing waves (Knobloch 1986). A codimension-2 bifurcation occurs at the location in parameter space where the stationary and the oscillatory instabilities meet, a fact which attracted even more interest from the mathematical side (see e.g. Knobloch & Proctor 1981; Coullet & Spiegel 1983; Brand, Hohenberg & Steinberg 1984). All these features have stimulated much theoretical and experimental interest in this system especially during the last decade. Early studies by Nield (1967), Hurle & Jakeman (1971), Legros *et al.* (1975), Chock & Li (1975) and others were followed by more specialized work. Experiments investigating the onset behaviour, such as determining the critical values and resolving the bifurcation structure in the linear and in the weakly nonlinear regimes, and also classifying the pattern variety in the strongly nonlinear range (Lee, Lucas & Tyler 1983; Walden *et al.* 1985; Rehberg & Ahlers 1985; Moses & Steinberg 1986; Kolodner *et al.* 1986*a*, 1987; Sullivan & Ahlers 1988; Lhost & Platten 1988, 1989; Steinberg *et al.* 1989; Bensimon *et al.* 1990; Kolodner, Glazier & Williams 1990; Schöpf & Rehberg 1992) have motivated much effort towards a theoretical understanding of the various features (Brand & Steinberg 1983; Knobloch 1986; Linz & Lücke 1987; Knobloch & Moore 1988; Cross & Kim 1988; Schöpf & Zimmermann 1989, 1990, 1993; Barten *et al.* 1989).

The fact that pattern-forming instabilities share many similarities has resulted in their universal description through the general concept of amplitude equations. This weakly nonlinear approach has been very successful since the pioneering work of Newell & Whitehead (1969), who first introduced it for the case of a stationary bifurcation. Here the derived amplitude equation has the same form as the Ginzburg–Landau equation known from the theory of phase transitions. Following Stewartson & Stewart (1971) and Newell (1974), amplitude equations have also been applied to systems showing a Hopf bifurcation. They are now often called generalized or complex Ginzburg–Landau equations, because in this case complex coefficients are involved. For quasi-one-dimensional systems in particular, where the amplitude depends only on one spatial coordinate, this concept has been used for investigating

the rich scenario near the onset of binary-fluid convection. Through qualitative studies of the solution variety of these equations (Bretherton & Spiegel 1983; Cross 1986, 1988; Thual & Fauve 1988; van Saarlos & Hohenberg 1990; Schöpf & Kramer 1991) and by calculating the respective coefficients describing the real system (Brand, Lomdahl & Newell 1986; Cross & Kim 1988; Schöpf & Zimmermann 1989, 1990) considerable progress in understanding the experimental features has been achieved.

In the neighbourhood of a hydrodynamic instability the fluid behaviour is very sensitive to perturbations. If external noise can be made small enough, so that the only remaining noise source is given by thermal fluctuations, these can be expected to manifest themselves macroscopically on length and time scales governed by the most unstable mode. This behaviour is reminiscent of equilibrium systems, where the appearence of macroscopic fluctuations close to a phase transition is well-known (see e.g. Stanley 1971). The basic idea for modelling intrinsic thermal fluctuations within the continuum description of fluid dynamics was introduced by Landau & Lifschitz (1957). The application to a concrete problem, namely the Rayleigh–Bénard system, was carried out about 20 years ago (Zaĭtsev & Shliomis 1970; Graham 1974). Linear theories predict a divergence of the fluctuations at the bifurcation, so that in the vicinity of this point nonlinear interactions of the modes have to be taken into account (Graham & Pleiner 1975). The most interesting outcome of a nonlinear analysis is the so-called Brazovskii effect, in which the interaction of a large number of modes can change the nature of the onset of convection from a supercritical to a subcritical bifurcation (Swift & Hohenberg 1977; Hohenberg & Swift 1992). This effect occurs only in an extremely small neighbourhood of the critical point.

While the statistical description of fluctuations in thermodynamic equilibrium is well-established in theoretical physics, hydrodynamic instabilities occur in non-equilibrium systems where the situation is less clear. Experimental investigations are therefore highly desirable for verifying the theoretical predictions. From the early calculations, however, it was evident that the influence of thermal noise on hydrodynamic bifurcations is so small that it hardly would be observed directly. Light scattering was proposed as the most powerful experimental method (see Lekkerkerker 1975), a technique which indeed could demonstrate the existence of fluctuations below the onset of electrohydrodynamic convection in a nematic liquid crystal (Smith *et al.* 1975), but without achieving a quantitative measurement of the fluctuation intensity. The results of another experiment by Pedersen & Riste (1980) using neutron scattering techniques in a similar system were even harder to interpret. The first quantitative measurements were done indirectly by using the exponential growth of the fluctuations after an increase of the temperature difference from subcritical to supercritical values by Ahlers *et al.* (1981) and Meyer, Ahlers & Cannell (1991), who succeeded in observing fluctuating convection patterns in the Rayleigh–Bénard system. The observed behaviour was indeed analogous to that predicted theoretically, but the measured fluctuations could only be explained by noise with a strength several orders of magnitude too large to be of thermal origin. It was only recently that the influence of thermal noise on the onset of convection was directly demonstrated in the electrohydrodynamic instability of a nematic liquid crystal by Rehberg *et al.* (1991 *a*, *b*) and, using an intrinsic amplification mechanism, also in binary fluid mixtures by Schöpf & Rehberg (1992).

This latter experiment is the topic of the present paper. The influence of thermal noise on the Hopf bifurcation is investigated in a quasi-one-dimensional system, which is achieved by using a very narrow convection channel, and therefore allows the description by a one-dimensional Ginzburg–Landau equation. The observation of the

noise-induced convection structures is made possible by the intrinsic amplification of the perturbations via the so-called convective instability, together with a drastically reduced reflection ability and a very sensitive measurement method. Section 2 briefly summarizes the theoretical efforts made in order to understand the influence of thermal noise and the results needed to interpret our experiments. In § 3 the experimental apparatus, the shadowgraph method used for quantitative observations and the measurement method are described in detail. The nature of the convective instability is explained in § 4, followed by a description of the influence and a measurement of the reflection coefficient. Furthermore some coefficients of the amplitude equation are obtained. The new results involving the noise-induced convection patterns are given in § 5. The observed small-amplitude travelling waves are discussed and their strength, obtained by calculating the temporal correlation function, is compared with the theoretical results. Finally, the significance of the experimental results and some corrections to our preceding paper (Schöpf & Rehberg 1992) are considered in the closing discussion in § 6.

## 2. The implementation of thermal noise in the theoretical description

A technique for including theoretically the always present thermal noise into the fundamental hydrodynamic equations has already been shown by Landau & Lifshitz (1957). The currents included in these equations have to be expanded by adding stochastic terms which describe the thermal fluctuations. The hydrodynamic equations in their normally known forms are simply equations for the averages of the unknown variables. The actual expressions for these new terms have also been given by Landau & Lifshitz (1957) for the usual one-component Rayleigh–Bénard convection and by Khalatnikov (1957) for the case of binary fluid mixtures. (Strictly speaking, Khalatnikov was interested in how hydrodynamic fluctuations influence the behaviour of a superfluid liquid, and obtained equations which are very similar to those governing binary fluid mixtures.) The fundamental equations to be considered in the latter case are written in non-dimensional form (see also Lekkerkerker & Laidlaw 1977; Schöpf & Zimmermann 1993) as

$$(\partial_t - \nabla^2)\vartheta - R\,\partial_x\phi = (\partial_z\phi\,\partial_x - \partial_x\phi\,\partial_z)\vartheta - \partial_i q_i, \tag{2.1a}$$

$$(\partial_t - L\nabla^2)\eta + \partial_t\vartheta - R\,\partial_x\phi = (\partial_z\phi\,\partial_x - \partial_x\phi\,\partial_z)(\eta + \vartheta) - \partial_i j_i, \tag{2.1b}$$

$$(\partial_t\nabla^2 - Pr\nabla^4)\phi - Pr\,\psi\,\partial_x\eta - Pr(1+\psi)\,\partial_x\vartheta = (\partial_z\phi\,\partial_x - \partial_x\phi\,\partial_z)\nabla^2\phi - \partial_z(\partial_i\sigma_{xi}) + \partial_x(\partial_i\sigma_{zi}). \tag{2.1c}$$

Here, summation over repeated indices is assumed. $\vartheta$, $\eta$ and $\phi$ represent the temperature field, the concentration field and the stream function, respectively, while $L = D/\kappa$ is the Lewis number, $Pr = \nu/\kappa$ the Prandtl number, $\psi = \beta k_T/\alpha T_0$ the separation ratio and $R = \alpha g d^3\Delta T/\kappa\nu$ the Rayleigh number (see below). The thermal fluctuations are described by the terms involving $q_i$, $j_i$ and $\sigma_{ij}$ on the right-hand sides of (2.1*a–c*) through their spatio-temporal autocorrelation functions given by

$$\langle q_i(r,t)q_j(r',t')\rangle = 2Q_1\,\delta_{ij}\delta(r-r')\delta(t-t'), \tag{2.2a}$$

$$\langle \sigma_{ij}(r,t)\sigma_{lm}(r',t')\rangle = 2Q_2\,(\delta_{il}\delta_{jm} + \delta_{im}\delta_{jl})\delta(r-r')\delta(t-t'), \tag{2.2b}$$

$$\langle j_i(r,t)j_j(r',t')\rangle = 2Q_3\,\delta_{ij}\delta(r-r')\delta(t-t'). \tag{2.2c}$$

The $Q_i$ are the strengths of the temperature, the velocity and the concentration fluctuations, respectively:

$$Q_1 = k_B T_0^2 \frac{g^2\alpha^2 d^3}{\nu^2\kappa^2\rho_0 c_p}, \qquad Q_2 = k_B T_0 \frac{\nu}{d\kappa^3\rho_0}, \qquad Q_3 = k_B T_0 \frac{D}{(\partial\mu/\partial c)\psi^2} \frac{g^2\beta^2 d^3}{\nu^2\kappa^3\rho_0}. \quad (2.3)$$

The parameters involved here are the Boltzman constant $k_B$, the mean working temperature $T_0$, the gravity force $g$, the thermal expansion coefficient $\alpha$, the height of the fluid layer $d$, the kinematic viscosity $\nu$, the thermal diffusivity $\kappa$, the fluid density $\rho_0$, the heat capacity $c_p$, the mass diffusivity $D$, the expansion coefficient due to concentration variations $\beta$ and the variation of the chemical potential $\mu$ with the concentration $c$. The remaining parameters needed for defining the non-dimensional numbers $L$, $P$, $\psi$ and $R$ are the temperature difference $\Delta T$ and the Soret coefficient $k_T$.

As mentioned in the introduction, the investigation of the bifurcation behaviour can be simplified by introducing amplitude equations valid near the convection onset. This is particularly useful for the quasi-one-dimensional system discussed here, because a relatively simple equation involving only one spatial coordinate is sufficient. The derivation of this equation from the fundamental hydrodynamic equations was explained in detail by Graham (1974), who showed how to include the terms describing the thermal fluctuations for the case of a simple fluid with free-slip boundary conditions. Following this work, the analogous equations valid for binary fluid mixtures with realistic boundary conditions were recently derived by Schöpf & Zimmermann (1993). In the case of a Hopf bifurcation leading to travelling-wave behaviour the following complex stochastic amplitude equation has to be used:

$$\tau_0(\partial_t - v_g\partial_x)A_0 = \varepsilon(1 + \mathrm{i}c_0)A_0 + \xi_0^2(1 + \mathrm{i}c_1)\partial_x^2 A_0 - (\alpha + \mathrm{i}c_2)|A_0|^2 A_0 + Q^{\frac{1}{2}}F(x,t). \quad (2.4)$$

Here $\varepsilon = (R - R_c)/R_c$ is the rescaled control parameter representing the relative distance from the convection onset, which occurs at $R_c$. The strength of the noise term $Q^{\frac{1}{2}}$ is determined by a combination of the $Q_i$ given in (2.3) and appearing in the basic equations (2.1*a–c*), and also involves the linear eigenfunctions at onset (Schöpf & Zimmermann 1993). The autocorelation function of the noise term is given by

$$\langle F^*(x,t)F(x',t')\rangle = \delta(x - x')\delta(t - t') \quad \text{and} \quad \langle F(x,t)F(x',t')\rangle = 0. \quad (2.5)$$

With these results the strength of the noise term can now be calculated for arbitrary combinations of the fluid parameters.

When applying (2.4) to convective states with very small amplitudes, which are expected to occur near the convection onset, the nonlinear term can be neglected in the first instance. In this case, the space-time correlation function of the noise-induced convection amplitude allows an analytical expression (see Rehberg *et al.* 1991*b* and Schöpf & Rehberg 1992; the derivation is given by Schöpf & Zimmermann 1993):

$$f_{cor}(A_0, \Delta x, \Delta t) := \langle A_0^*(x,t)A_0(x + \Delta x, t + \Delta t)\rangle = \tfrac{1}{2}\hat{A}_0^2\, \mathrm{e}^{\mathrm{i}c_1\Delta t/t_0}$$
$$\times \left\{ \mathrm{e}^{-\left(\frac{\Delta x}{x_0} + \frac{\Delta t}{t_1}\right)} \mathrm{erfc}\left( \left(\bar{c}_1 \frac{\Delta t}{t_0}\right)^{\frac{1}{2}} - \frac{1}{2(\bar{c}_1)^{\frac{1}{2}}} \left( \frac{\Delta x/x_0}{(\Delta t/t_0)^{\frac{1}{2}}} + \left(\frac{t_0 \Delta t}{t_1^2}\right)^{\frac{1}{2}} \right) \right) \right.$$
$$\left. + \mathrm{e}^{+\left(\frac{\Delta x}{x_0} + \frac{\Delta t}{t_1}\right)} \mathrm{erfc}\left( \left(\bar{c}_1 \frac{\Delta t}{t_0}\right)^{\frac{1}{2}} + \frac{1}{2(\bar{c}_1)^{\frac{1}{2}}} \left( \frac{\Delta x/x_0}{(\Delta t/t_0)^{\frac{1}{2}}} + \left(\frac{t_0 \Delta t}{t_1^2}\right)^{\frac{1}{2}} \right) \right) \right\}. \quad (2.6)$$

Here the abbreviations $\hat{A}_0^2 := |Q|/4\tau_0\xi_0(-\varepsilon)^{\frac{1}{2}}$, $x_0 := \xi_0/(-\varepsilon)^{\frac{1}{2}}$, $t_0 := \tau_0/(-\varepsilon)$, $t_1 :=$

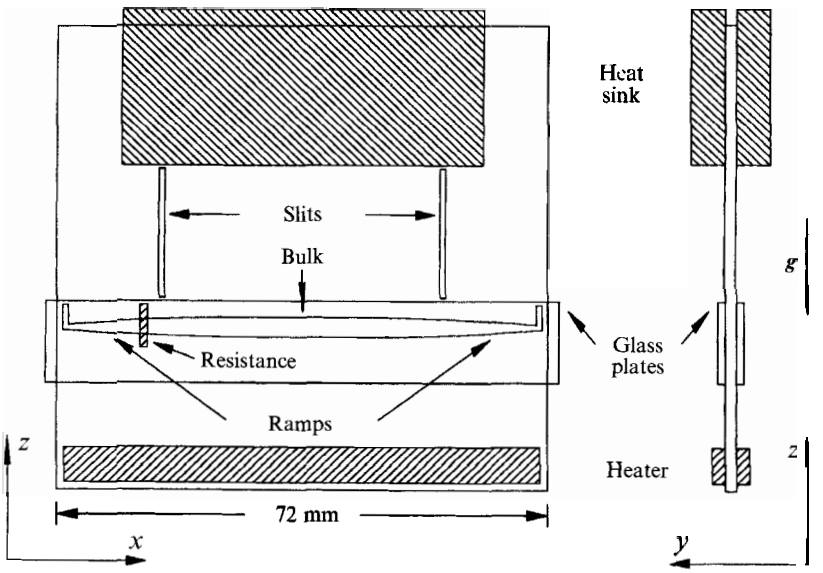


FIGURE 1. The convection channel is cut out of a copper plate of dimensions $72 \times 72 \times 1.5$ mm$^3$. This sketch views it from the front side and, on the right, also from the narrow side. The system of coordinates as used in this paper is indicated in the lower left- and right-hand corners, respectively. The gravity force g acts downwards as shown by the arrow at the right-hand margin. The apparatus is explained in detail in the text.

$\xi_0/v_g(-\varepsilon)^{\frac{1}{2}}$ and $\bar{c}_1 := 1 + ic_1$ have been introduced. The intensity $\hat{A}_0^2$, which includes only known quantities, can be rescaled into the intensity for the temperature correlation $\hat{T}^2$ to be compared with the experimentally measured value. This will be done and discussed in detail in § 5.

## 3. Experimental setup

### 3.1. *Convection channel and thermal stability*

Figure 1 is a sketch of the experimental apparatus (also called *convection cell*) from the front side and, rotated by 90°, also from the narrow side. The direction of the gravity force g is indicated by the arrow on the right-hand side, and the coordinate system is shown in the lower right- and left-hand corners. The apparatus is made from a square copper plate of lateral dimensions 72 mm and thickness 1.5 mm. The convection channel to contain the fluid is cut out of the copper plate in the middle part. It consists of a spatially homogeneous *bulk* region of length 18 and height 3 mm, thus allowing for about three pairs of convection rolls. Adjacent to this part, where the top and bottom boundaries are parallel, subcritical parabolic *ramps* smoothly reduce the height of the channel from 3 to 1 mm over a length of 26 mm on both sides. The convection channel is closed at the front and back sides by means of glass plates, which are glued onto the copper basis. Well inside the ramped part, a resistor used for generating heat pulses (see § 4) is attached to the outer side of one of the glass plates.

The top of the copper plate is in thermal contact with a water circuit of constant temperature (*heat sink* in figure 1). The convection channel is electrically heated from below by applying a constant voltage $U_{heat}$ to a constantan wire wound around the

bottom of the copper plate (*heater* in figure 1). The resultant temperature difference between the upper and lower boundary of the fluid is measured via six thermocouples (copper–constantan) connected in series, which are attached to the copper plate near the convection channel (not shown in figure 1). To keep horizontal temperature gradients in the bulk part to a minimum, two slits of width 1 mm are cut into the copper above the channel.

If not otherwise stated, a mixture of water and ethanol at a mean temperature of 30 °C consisting of 22.04 wt-% ethanol was used to fill the convection channel for our experiments. For this fluid the characteristic parameters are a Prandtl number of $Pr = 15.5$, a Lewis number of $L = 0.009$ and a separation ratio of $\psi = -0.125$ (from Kolodner, Williams & Moe 1988).

The described convection apparatus has two special features. Firstly, complicated three-dimensional convection currents are avoided by using a narrow channel with a height-to-width ratio of 2 in the bulk regime. The fluid flow is confined to the $(x, z)$-plane, while the $y$-dependence can be approximated by a parabolic Poiseuille flow (see e.g. Frick & Clever 1980; Schöpf 1992). Secondly, a convection pattern, which is well-developed inside the bulk part, becomes subcritical inside the ramps because of the decreasing height corresponding to a decreasing Rayleigh number. Hence, travelling waves will vanish when propagating into the ramps, a fact that drastically reduces the reflection from the left- and right-hand boundaries (for details see § 4).

At this point it is worth discussing the possibility of a mean flow inside the convection channel, which might be due to the ramped geometry. If there were only one ramp, for instance in the lower part of the left-hand side of the channel, a clockwise rotation would be induced. The curving of the upper part on the other hand should lead to a counter-clockwise rotation of the mean flow. In order to minimize such effects, the ramps were made mirror symmetric on top and bottom. Still, a large-scale flow pattern induced by this geometry cannot be excluded. Presumably, this would have the form of two counter-rotating rolls sitting on top of each other, with their lengthscale given by the extent of the ramp. In the experiments, however, neither this pattern nor any other mean flow was detected. Also the deterministic rolls created at supercritical values of the temperature difference did not appear unusual or asymmetric. Therefore, we believe that any possibly present mean flow is only a small correction to the linear equations describing the rolls.

Great care has been taken to ensure the stability of the experimental parameters. The apparatus is fitted into a cylindrical aluminium box in such a way, that the top of the copper plate (*heat sink* in figure 1) is in thermal contact with the lid of the box, which is temperature regulated by the cooling water circuit. The aluminium cylinder is embedded in a box made from styrofoam of thickness 2 cm, which itself is embedded in another styrofoam box. The gap between these two boxes is also maintained at a constant temperature by the water circuit, so that the whole arrangement can be considered a very well insulated isothermal box. By introducing an additional regulation into the water circuit just before entering the aluminium box, a long-time stationarity of the temperature at the convection cell of better than $\pm 0.003$ °C is achieved. For electrically heating the convection channel from below, an adjustable regulated highly constant power supply is used. This and the temperature regulation for cooling are stored inside an isothermal box, in order to eliminate the variations which electronic parts usually experience with varying temperature.

The results of these efforts are shown in figure 2, where the temperature of the lid of the aluminium box (*a*), the voltage for heating from below (*b*), and the

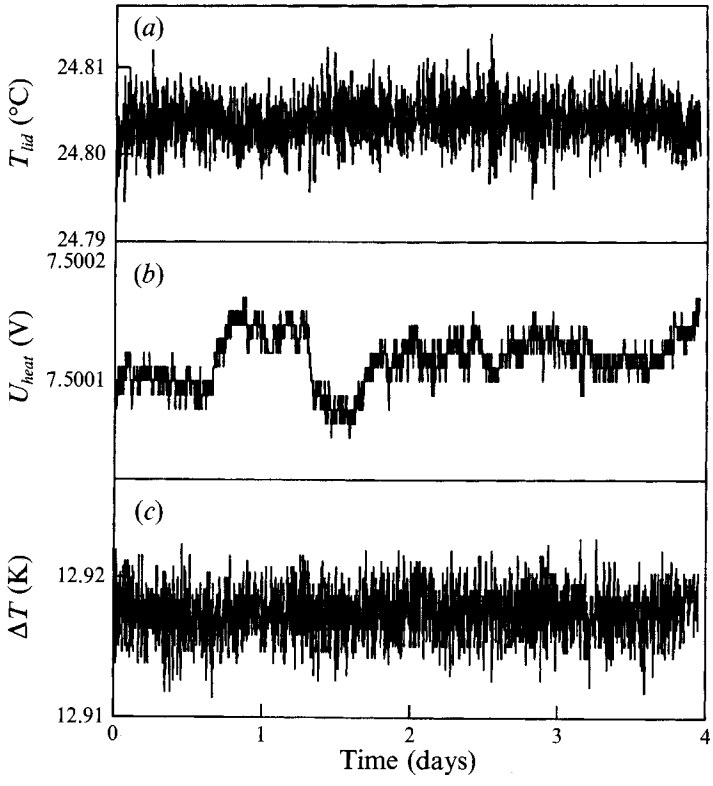


FIGURE 2. Long-time stability of the important externally controlled parameters applied to the convection cell. Shown as functions of time for about four days are (*a*) the temperature of the lid of the aluminium box, (*b*) the voltage used for heating from below, and (*c*) the temperature difference between the top and bottom boundaries of the fluid.

temperature difference applied to the fluid (*c*) are given as functions of time for about four days. The lid temperature $T_{lid} = (24.8038 \pm 0.0026)\,^{\circ}\mathrm{C}$ is constant to within 3 mK. The heating voltage $U_{heat} = (7.50012 \pm 0.00002)$ V varies only in the last digit of the multimeter and can be considered as perfectly constant for our purposes. The resulting temperature difference $\Delta T = (12.9175 \pm 0.0018)$ K is constant to within 2 mK, corresponding to a relative stability better than 0.014 %. Here the problem of measuring very small voltages arises, since the thermocouples yield $U_{ther} \approx (2\text{–}3) \times 10^{-3}$ V, which is of the same order of magnitude as the accuracy of the multimeter. It can therefore be assumed that the actual variation of the temperature difference is even smaller, which is also suggested by the stability of the lid temperature and the heating voltage. The precision of this measurement could in principle be improved by using a larger number of thermocouples, but this approach is made difficult by the restricted space on the copper plate.

### 3.2. *Optical setup and shadowgraph method*

The optical setup is schematically sketched in figure 3. A white point light source is generated by putting a pinhole in front of a halogen lamp. The light is made weakly convergent by means of a (chromatically corrected) lens of focal length 1 m and the resulting light beam illuminates the $(x, z)$-plane of the convection channel. The images are taken by a black-and-white CCD–camera which focuses about 2 m

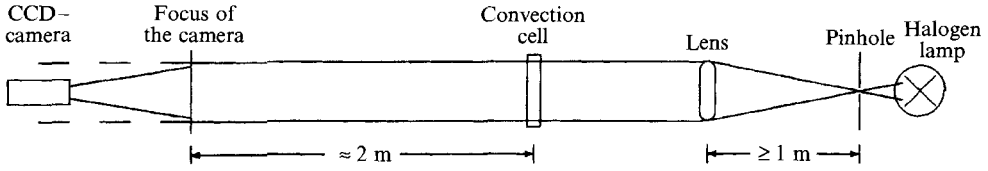


FIGURE 3. Schematical sketch of the optical setup. White light coming from a halogen lamp is made weakly convergent by means of a lens and illuminates the convection channel from the front side ($x, z$-plane). The resulting images taken by the CCD–camera are further processed using frame-grabbing facilities implemented in a PC/AT–computer (not shown here).

behind the apparatus. In order to minimize mechanical disturbances, the whole setup sits on an optical table which consists of a granite plate of thickness 15 cm lying on two large styrofoam blocks. A black-painted wooden shell covers the setup to ensure optical insulation from the surroundings.

Flow visualization of the convection patterns is achieved by the well-known *shadowgraph* technique (see e.g. Busse & Whitehead 1971, 1974). This inexpensive, easy-to-handle but extremely sensitive method has proven very successful for application in fluid flows involving thermal gradients (see e.g. Heutmaker, Fraenkel & Gollub 1985; Steinberg, Ahlers & Cannell 1985; Kolodner *et al.* 1986*b*; Croquette & Williams 1989). The principles are rather simple: the convection rolls consisting of warm ascending and cold descending fluid lead to a spatially modulated temperature gradient, which manifests itself optically as a spatial modulation of the refractive index of the fluid and hence can be made visible. The method is explained in detail by Rasenat *et al.* (1989). For our setup the shadowgraph image is the result of a spatial integration over the entire width of 1.5 mm of the convection channel, which makes the method most appropriate for observing the expected quasi-one-dimensional structures. By using a frame-grabber board, the shadowgraph image taken by the CCD–camera is digitized into an array of 512 × 512 pixels of 8-bit grey-scale values, which is stored and further processed by a PC/AT–computer.

In this experiment we are mainly interested in very small convection amplitudes leading to very small variations in grey scale. Furthermore, our observation point is located far away from the caustics produced by the shadowgraph method as discussed by Rasenat *et al.* (1989). Since in this case the technique always works inside its linear regime, the general full nonlinear calculation performed by Rasenat *et al.* (1989) is not necessary here and can be replaced by the following simplified estimation.

Consider the setup sketched in figure 4, where a transparent object of thickness $l$ is illuminated by a parallel light beam. The variation of the refractive index $n(x)$ inside the object is assumed to focus the light to a point at a distance $f$ behind the object. With $s(x)$ being the length of a possible light path from the object to the focal point and $L(x) = l\,n(x)$ being the length of the optical light path inside the object, Fermat's principle yields $s(x) + L(x) = \text{const}$. Besides this, $s(x)$ is also given by $s^2 = f^2 + x^2$ which can be approximated by $s(x) \approx f + x^2/2f$, as long as the lateral dimensions of the object are small compared to the focal length, i.e. $x \ll f$. Combining the latter expression with Fermat's principle, we find for the focal length

$$\frac{1}{f} = -\frac{\partial^2 L}{\partial x^2} = -l\frac{\partial^2 n}{\partial x^2}. \tag{3.1}$$

Let the object of figure 4 now be a pair of convection rolls. In a vicinity of the

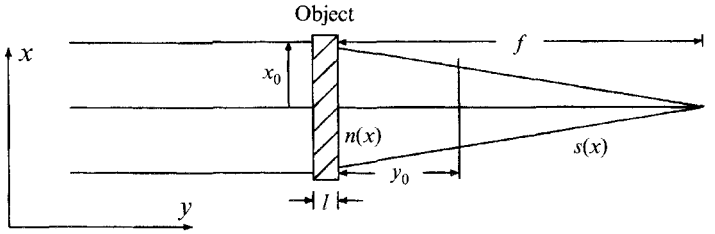


FIGURE 4. Principles of the shadowgraph technique as used in our experiment. The refractive index $n(x)$ of a transparent object is assumed to vary in such a way that an incoming parallel light beam is focused to a point at a distance $f$ behind the object. $s(x)$ is the length of a possible light path from the object to the focal point and $x_0$ is the lateral dimension of the object with $x_0 \ll f$. The light intensity is measured at a distance $y_0$ behind the object. The system of coordinates is indicated at the left-hand side. See text for details of the calculation.

descending fluid, this can be treated locally as a lens with focal length $f_c$. A purely geometrical consideration yields the relative change in light intensity at a distance $y_0$ behind the object as $(\Delta I/I) = y_0/(f_c - y_0)$, where $I$ is the mean intensity of the incoming light beam. Hence, the focal length of the convection roll is given by

$$\frac{1}{f_c} = \frac{1}{y_0}\left(\frac{\Delta I}{I}\right)\left(1+\frac{\Delta I}{I}\right)^{-1} \approx \frac{1}{y_0}\left(\frac{\Delta I}{I}\right). \tag{3.2}$$

The approximation in the last step is justified by the experimentally measured values of $(\Delta I/I) \approx (10^{-4}\text{–}10^{-2})$.

The result (3.2) holds for illumination with parallel light, whereas in our experiment weakly convergent light was used instead. Without convection (i.e. no lateral variations of the refractive index) this leads to a focus at a distance $f_0$ behind the apparatus, while in the presence of convection the focal length is given by $f_g$ with $f_g^{-1} = f_0^{-1} + f_c^{-1}$. Again, a geometrical consideration yields $(\Delta I/I) = (f_0 - f_g)y_0/(f_g - y_0)f_0$ with $I$ now being the mean intensity at the measurement point $y_0$. The focal length of the convection roll is then given by

$$\frac{1}{f_c} = \frac{f_0 - y_0}{f_0 y_0}\left(\frac{\Delta I}{I}\right)\left(1+\frac{\Delta I}{I}\right)^{-1} \approx \frac{f_0 - y_0}{f_0 y_0}\left(\frac{\Delta I}{I}\right). \tag{3.3}$$

Interpreting this as the value given by (3.1), the dependence of the refractive index on convection can be expressed by the measured change of the relative light intensity via $l\,(\partial^2 n_c/\partial x^2) = -[(f_0 - y_0)/(f_0 y_0)](\Delta I/I)_{exp}$.

Near the convection onset the refractive index inside the fluid varies periodically with the critical wavenumber $k_c$ around its mean value $n_0$: $n_c(x) = n_0 + \Delta n(x)$ with $\Delta n(x) = A \sin k_c x$. Hence, $(\partial^2 n_c/\partial x^2) = -k_c^2\,\Delta n(x)$ and with $k_c = 2\pi/\lambda_c$ we eventually find

$$\Delta n(x) = \frac{\lambda_c^2}{4\pi^2 l}\frac{f_0 - y_0}{f_0 y_0}\left(\frac{\Delta I}{I}\right)_{exp}. \tag{3.4}$$

Inserting the experimental values $y_0 \approx 2$ m, $f_0 \approx 8$ m, $\lambda_c \approx 5.3$ mm and $l = 1.5$ mm, the variation of the refractive index due to convection is given by the measured change of the relative light intensity through

$$\Delta n(x) \approx 0.00018\left(\frac{\Delta I}{I}\right)_{exp}. \tag{3.5}$$

In binary fluid mixtures, this is not only caused by the temperature distribution

inside the fluid, but also by the concentration distribution: $\Delta n(x) = (\Delta n/\Delta T)\,\Delta T(x) + (\Delta n/\Delta c)\,\Delta c(x)$. The variation of the refractive index with temperature can be found either by applying the Lorentz–Lorenz formula (see for example Lusty & Dunn 1987) or by interpreting direct measurements for the relevant temperature range (Kolodner *et al.* 1988). Both methods yield about the same result of $(\Delta n/\Delta T) \approx 2.05 \times 10^{-4}\ \mathrm{K}^{-1}$. The variation of the refractive index with concentration has also been measured by Kolodner *et al.* (1988), yielding $(\Delta n/\Delta c) \approx 0.063$ for our mixture. The temperature and the concentration fields, which are coupled by the fundamental hydrodynamic equations, can be described by the linear solutions at threshold for the extremely small amplitudes that we are interested in. When these fields are calculated as the integrals over the entire vertical extent of the channel as in our experiment (see § 3.3), the ratio between the temperature and the concentration is $\Delta T(x)/\Delta c(x) \approx 0.37$ in the dimensionless units used by Schöpf & Zimmermann (1993). After scaling this back to the relevant experimental units and taking into account the values of $(\Delta n/\Delta T)$ and $(\Delta n/\Delta c)$ from above, the variation of the refractive index turns out to be about 73% dependent on the temperature field and about 27% dependent on the concentration field. Since we eventually want to compare our results with the theoretical values obtained for the temperature variation (see § 5), we need to consider only the part given by the temperature field. Equation (3.5) yields, together with $(\Delta n/\Delta T) \approx 2.05 \times 10^{-4}\ \mathrm{K}^{-1}$, for the relevant 73% (in Kelvin)

$$\Delta T(x) \approx 0.64 \left(\frac{\Delta I}{I}\right)_{exp} \mathrm{K}. \tag{3.6}$$

Thus, the relative intensity variations taken from the shadowgraph images can be used as a quantitative measure of the lateral temperature variations due to convection. The result (3.6), however, can only be applied to very small intensity variations, as caused e.g. by the convective states discussed in § 5, where the shadowgraph technique behaves linearly. For fully developed, highly nonlinear convection, the method can in our case only be interpreted for qualitative estimates.

### 3.3. *Measurement method and stability diagram*

Through the frame-grabbing procedures we get from the shadowgraph image a two-dimensional grey-scale map $I(x, z)$ governing the entire convection channel. Since we are only interested in the $x$-dependence of the convective structures, we can integrate over the vertical dimension by adding together all horizontal lines to one line $I_c(x) = \int I(x, z)\,\mathrm{d}z$. This procedure not only increases the contrast of the image, but we also eliminate a mean vertical displacement of the convection channel caused by the fact that the vertical gradient of the refractive index varies with the applied temperature difference. In order to minimize optical inhomogeneities which may be due to uneven illumination or to other irregularities of the optical setup, the lines $I_c(x)$ are divided by a reference line $I_0(x)$ taken in a state without convection. The resulting lines $I_{pro}(x) = I_c(x)/I_0(x)$, called *profile lines* in the following, are the main basis for analysing the data. One individual profile line can be quantified by a single number, the *r.m.s.*-value

$$\bar{I}_{rms}(I_{pro}) = \left(\frac{1}{512}\sum_{i=1}^{512}\left(I_{pro}(x_i) - \bar{I}_{pro}\right)^2\right)^{\frac{1}{2}} \tag{3.7}$$

where $\bar{I}_{pro}$ is the mean value of the line. The *r.m.s.*-value $\bar{I}_{rms}$ and especially changes of this value can be used to some extent to analyse the convection behaviour. In a

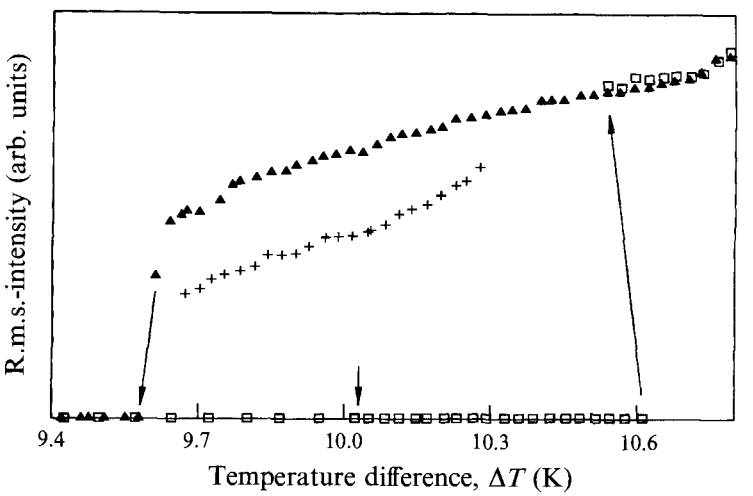


FIGURE 5. Stability diagram as measured for our working fluid. The *r.m.s.*-intensity $\bar{I}_{rms}$ of the respective profile lines is shown as a function of the applied temperature difference $\Delta T$ with open squares corresponding to increasing and closed triangles to decreasing $\Delta T$. The onset of nonlinear convection for $\Delta T_c = 10.61$ K is clearly visible. When reducing the temperature difference, convection does not vanish until the lower value of $\Delta T_s = 9.61$ K is reached, which is caused by the subcritical nature of the bifurcation leading to the observed hysteresis. The small arrow at $\Delta T_c^{con} = 10.03$ K indicates the onset of the convective instability, where the growth rate of a homogeneous disturbance is zero ($\varepsilon = 0$). The crosses inside the stability diagram correspond to stable localized travelling waves (confined states).

state without convection, $\bar{I}_{rms}$ should be zero so that its rise indicates the onset of convection.

Figure 5 shows the experimentally measured stability diagram for our working fluid. Here, $\bar{I}_{rms}$ is plotted versus the applied temperature difference. From a quiescent state without convection, the temperature difference was increased stepwise (open squares in figure 5) with an appropriate waiting time allowing a new steady state to establish after each step. The onset of nonlinear convection at $\Delta T_c = 10.61$ K ($\varepsilon_c = 0.058$) can clearly be seen. Owing to the subcritical nature of the bifurcation in this system, there exists no stable, weakly nonlinear state of small-amplitude convection, but rather the system develops via a transient stage into a state of strongly nonlinear convection. When reducing the temperature difference (closed triangles in figure 5), convection persists for values less than $\Delta T_c$, leading to the expected hysteresis until the value $\Delta T_s = 9.61$ K ($\varepsilon_s = -0.042$) is reached, where it abruptly ends. As already mentioned, the shadowgraph method behaves nonlinearly for the convective states observed here, hence no simple connection between $\bar{I}_{rms}$ and the temperature variation inside the fluid can be given. Therefore the units on the vertical axis of figure 5 are omitted; however, $\bar{I}_{rms} = 0$ on the bottom line.

The arrow at $\Delta T_c^{con} = 10.03$ K indicates the onset of the *convective* instability. Here the growth rate of a homogeneous disturbance is zero ($\varepsilon = 0$) and becomes positive for $\Delta T > \Delta T_c^{con}$. The character of this instability and the meaning of the measured values $\Delta T_c$ and $\Delta T_c^{con}$ will be discussed in §4. In the subcritical range $\Delta T < \Delta T_c$ we find linear propagating waves of extremely small amplitude, which will be discussed in detail in §5.

The onset of nonlinear convection via transient behaviour is very similar to that observed in other experiments in this system (see for example Kolodner *et al.* 1986*a*;

Lhost & Platten 1988). Upon reaching the critical temperature difference $\Delta T_c$, linear waves travelling with the Hopf frequency can be seen initially. The amplitude then rises exponentially until a saturation value is achieved, leaving a state of nonlinear convection with reduced frequency. The frequency will decrease even more and finally drop to zero on the upper branch of figure 5. On this branch, no travelling waves exist for any of the applied temperature differences; here convection always has the form of stationary rolls. This is in contrast to experiments in two-dimensionally extended systems, where at least in some range nonlinear travelling waves are found (Walden *et al.* 1985; Lhost & Platten 1988; Steinberg *et al.* 1989; Bensimon *et al.* 1990). This is a special feature of our narrow channel, which obviously forces the stationarity of the rolls. One possible explanation is the relatively large thermal diffusivity of the glass plates, which carry away a considerable amount of heat and so decrease the effective Lewis number. In the nonlinear state, the mixture therefore behaves like a usual, one-component fluid, with the Soret effect acting too slowly to take care of the demixing. This is of course only a speculation, and a further investigation of this point would be very interesting.

The fairly long periods of the travelling waves ($\geqslant 25$ s) allow a very accurate measurement of the critical frequency from the linear states (see also § 5). In this way we get $\omega_c \approx 0.22$ Hz. The measurement of the wavelength of the convection rolls, however, is complicated by the shortness of the convection channel (only about 6 rolls fit into the bulk part) and also by the ramps, which cause a weak $x$-dependence of the wavelength. Through replacing the convection apparatus by a mm-scale under otherwise equal conditions, we found inside the bulk regime a value of $\bar{\lambda}_c \approx 5.3$ mm corresponding to a non-dimensional wavenumber of $\bar{k}_c \approx 3.56$.

### 3.4. *Stable confined states*

The crosses in the stability diagram of figure 5 correspond to stable localized travelling waves, where convection takes place only in one part of the channel, while the remaining fluid is quiescent. These states are the same as the 'fast confined states' found by Bensimon *et al.* (1990). We find for the range of their existence $\Delta\varepsilon_{cs} \approx 0.06$, which is considerably larger than the value of $\Delta\varepsilon_{cs} \approx 0.015$ measured by Bensimon *et al.* (1990) in an annular geometry (note that the value of $\Delta r = 0.023$ given by those authors is scaled with respect to the onset of instability in a *pure* fluid).† Upon increasing the temperature difference above $\Delta T = 10.28$ K (right-most cross in figure 5), the state will extend to fill the whole channel with rolls, while decreasing it below $\Delta T = 9.67$ K (left-most cross in figure 5) will force the convection to vanish.

Some more results were obtained using a mixture of 17 wt-% ethanol in water at a mean temperature of 30 °C. Following Kolodner *et al.* (1988), this mixture corresponds to $L = 0.0083$, $Pr = 12.81$ and $\psi = -0.183$. We found $\Delta T_s = 9.0$ K, $\Delta T_c^{con} = 9.8$ K and $\Delta T_c = 10.46$ K, and $\omega_c = 0.27$ Hz for the Hopf frequency. Confined states could be observed for temperature differences between $\Delta T = 9.17$ and 9.83 K corresponding to a range of existence of $\Delta\varepsilon_{cs} \approx 0.067$. For the frequencies of the localized travelling waves we measured $\omega_{cs} = 0.08$ Hz $\approx 0.3\omega_c$ at $\Delta T = 9.17$ K, $\omega_{cs} = 0.067$ Hz $\approx 0.25\omega_c$ at $\Delta T = 9.43$ K and $\omega_{cs} = 0.047$ Hz $\approx 0.17\omega_c$ at $\Delta T = 9.83$ K, which are obviously different from the linear result. The fact that the frequency decreases with increasing

† Recent experiments performed by Kolodner (1993) in an extremely uniform annular convection cell showed that the range of existence of a confined state with a given width is in fact zero. In another experiment using a fluid with $\psi = -0.127$, stable narrow confined states (*pulses*) have been observed over a range of $\Delta\varepsilon = 0.034$ (private communication by P. Kolodner).

temperature difference is in agreement with experimental results obtained by Steinberg *et al.* (1989) and Bensimon *et al.* (1990).

## 4. Convective instability and reflection behaviour

### 4.1. *Convective and absolute instability*

In systems showing propagating modes, the distinction between *convective* and *absolute* instability becomes important (see e.g. Landau & Lifshitz 1959; Akhiezer & Polovin 1971; Huerre & Monkewitz 1985). These concepts are well-known from Poiseuille flow through a pipe, from plasma instabilities, and from applications in other open-flow systems (see e.g. Landau & Lifshitz 1959; Briggs 1964; Deissler 1985). They were first introduced to binary-fluid convection in an attempt to explain the still not fully understood confined states (Cross 1986, 1988). The idea can be illustrated qualitatively by following the development of a localized disturbance in an otherwise quiescent state. Owing to the non-vanishing group velocity arising in the systems of interest this perturbation will be carried through the system, in the course of which it can undergo three basic types of qualitatively different modifications. If the value of the control parameter is such that the amplitude of the disturbance decreases while being carried away, it will eventually vanish and the system is thus *stable*. If, on the other hand, the amplitude increases as the disturbance moves on but nevertheless will vanish for every fixed position when this position has been passed, the system is called *convectively unstable*. Finally, for a sufficiently high value of the control parameter each disturbance can grow so fast that despite being carried away it will extend over the entire system, corresponding to a situation of *absolute instability*.

A quantitative understanding of these concepts can be gained most simply by analysing the amplitude equation for example for the amplitude $A$ of a left-travelling wave (see Deissler 1985):

$$\tau_0(\partial_t - v_g\partial_x)A = \varepsilon(1 + \mathrm{i}c_0)A + \xi_0^2(1 + \mathrm{i}c_1)\partial_x^2 A - (\alpha + \mathrm{i}c_2)|A|^2 A. \tag{4.1}$$

When looking for the linear stability of the solution $A = 0$ against homogeneous disturbances of the form $u\exp(\mathrm{i}(Qx + \Omega t))$, it is apparent that the amplitude $u$ of the disturbance will decrease exponentially for $\varepsilon < 0$, determining the linear stability boundary as $\varepsilon_c = 0$. When, however, investigating the stability against a localized perturbation, a distinction analogous to the qualitative behaviour discussed above can be found, hence showing that an infinitely extended system is (Deissler 1985)

$$\text{stable for} \quad \varepsilon < \varepsilon_c^{con} = 0, \tag{4.2a}$$

$$\text{convectively unstable for} \quad \varepsilon_c^{con} < \varepsilon < \varepsilon_c^{abs}, \tag{4.2b}$$

$$\text{absolutely unstable for} \quad \varepsilon > \varepsilon_c^{abs} = \left(\frac{v_g\tau_0}{2\xi_0}\right)^2 \frac{1}{1 + c_1^2}. \tag{4.2c}$$

A stability analysis of the fundamental hydrodynamic equations, as performed for the case of binary fluid mixtures e.g. by Legros *et al.* (1975), Chock & Li (1975), Knobloch & Moore (1988), Cross & Kim (1988) or Schöpf & Zimmermann (1989), usually applies to homogeneous disturbances and thus yields the onset of the convective instability. The situation is slightly more complicated for finite systems where the solutions of interest have to be constructed from the respective eigenfunctions. It turns out that the boundaries have a weakly stabilizing influence, shifting the absolute instability by an amount of the order $l^{-2}$ from $\varepsilon_c^{abs}$ to some $\varepsilon_c^{abs,fin}$, when $l$ is the length of the system (Deissler 1985).

In an experiment, the actual onset of the instability depends on the geometry of the apparatus as well as on the nature of the disturbances. When dealing with permanently arising, stochastic fluctuations, which may for example be due to thermal noise and are therefore always present, the difference between the onset of the convective instability and the onset of the absolute instability will not necessarily manifest itself in an infinitely extended system. The same is true for an annular geometry, where additionally each single perturbation will always be carried back to its origin. Obviously the full range of the convective instability $0 < \varepsilon < \varepsilon_c^{abs,fin}$ can only be investigated in a finite system showing no reflections from the sidewalls.

### 4.2. *The influence of the reflection coefficient*

In practice, reflection of the disturbances from the lateral boundaries will always lower the onset of nonlinear convection, thus occurring at some $\varepsilon_c^{ref} < \varepsilon_c^{abs,fin}$ before the absolute instability point of the finite system under consideration is reached. In this case the full calculation is more complicated because the finite system together with the boundary conditions has to be considered. However, for a not too small reflection coefficient $r$ and neglecting diffusion and dispersion effects which will decrease $\varepsilon_c^{ref}$, one can estimate it simply from the balance between the exponential growth during the propagation across the channel and the loss due to reflection at the boundaries (Cross 1986, 1988):

$$\varepsilon_c^{ref} = -\frac{v_g \tau_0}{l} \ln(r), \tag{4.3}$$

with $l$ being the system length. Under normal experimental conditions ($l \approx 20$ and $r \approx 0.4$, see e.g. Cross 1986; Kolodner *et al.* 1987) together with the relevant coefficients corresponding to our mixture ($v_g = 2.3$, $\tau_0 = 0.104$, $\xi_0^2 = 0.147$ and $c_1 = 0.09$, see Cross & Kim 1988; Schöpf & Zimmermann 1989) this yields $\varepsilon_c^{ref} \approx 0.01$, while from (4.2*c*) one finds $\varepsilon_c^{abs} \approx 0.1$. Hence the absolute instability is usually out of reach and in most experiments the onset of this reflection-induced instability is observed. This instability can be shifted towards higher values of the control parameter by for example decreasing the reflection coefficient as can be seen from (4.3). This is the reason for introducing into our convection channel the subcritical ramps shown in figure 1, which decrease the amplitude of waves travelling into these ramps and so effectively prevent reflection from the sidewalls. We find $\Delta T_c^{con} = 10.03$ K for the onset of the convective instability (see § 4.3), while the onset of nonlinear convection as discussed in § 3.3 occurring at $\Delta T_c =: \Delta T_c^{ref} = 10.61$ K now has to be interpreted as the onset of convection due to reflection. The value of

$$\varepsilon_{c,exp}^{ref} \approx 0.06 \tag{4.4}$$

so obtained is considerably larger than the value of 0.01 discussed above for conventional convection cells.

For demonstration purposes, but especially for measuring the actual value of the reflection coeffient and of $\Delta T_c^{con}$ (see § 4.3), the resistor shown in figure 1 inside one of the ramps is used. When applying a voltage for a short duration of time (a *voltage pulse*) to this resistor, inside the fluid a localized perturbation in the form of a *heat pulse* is generated, which is forced by the group velocity to travel through the system. Figure 6(*a*) shows in the form of a space–time plot the response of our system to one such disturbance. Profile lines taken at consecutive times for a duration of 12 minutes are drawn one above the preceding one. The resistor itself is located at $x \approx 7d$ and is not shown in figure 6(*a*). The temperature difference of $\Delta T = 10.34$ K corresponds to a positive value of $\varepsilon = 0.03$ in the bulk regime. The amplitude of the travelling

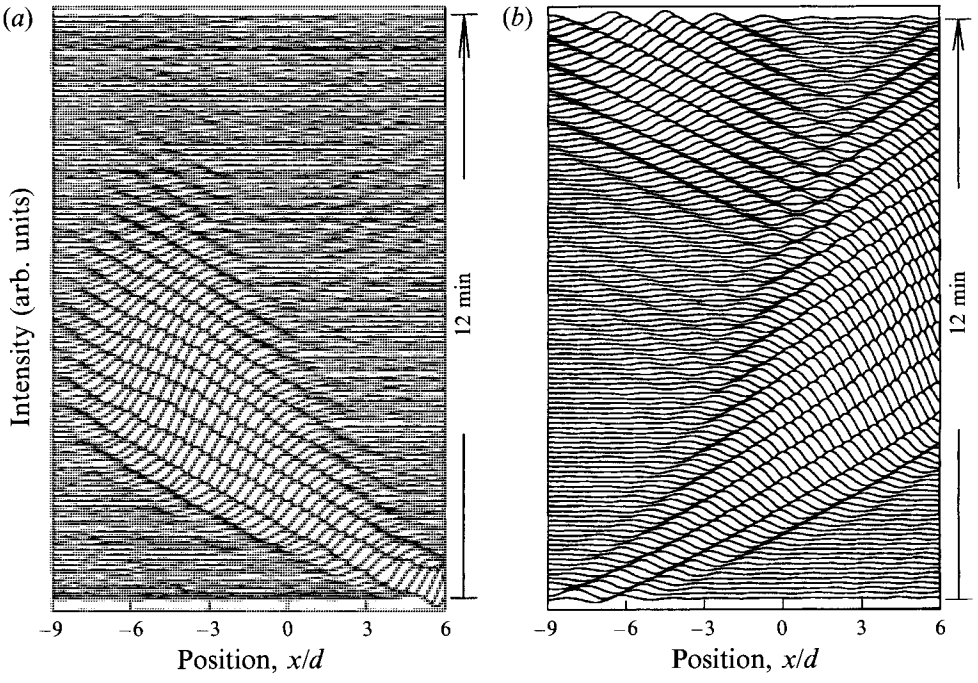


FIGURE 6. Space–time plot to demonstrate the reflection behaviour of the convection channel. For this sort of representation several profile lines taken consecutively in time are plotted one above the preceding one (here for a duration of 12 minutes altogether). A voltage pulse applied to the resistor shown in figure 1 generates a localized disturbance which penetrates through the channel. The measurements correspond to convectively but not absolutely unstable situations ($\varepsilon = 0.03$). The resistor for generating the heat pulse is located outside the plotted area on the right-hand on (*a*) and on the left-hand side on (*b*). (*a*) Convection cell used in our experiments as shown in figure 1 and explained in detail in the text with the homogeneous region extending between $x = \pm 3d$. A very weak reflected wave can be seen in the upper right part of the picture. (*b*) Rectangular convection cell similar to the one described in figure 1, but without ramps and instead the bulk part extended over the entire lateral dimension. Now the wave reflected from the right-hand boundary can clearly be recognized.

perturbation first decreases until the supercritical part of the channel is reached. Then it increases owing to the convectively unstable nature of the instability in the inner part of the cell before decreasing again inside the opposite ramp to eventually vanish at $x \approx -9d$. Note the spreading in time which is due to diffusion and dispersion. Only a very weak reflected wave can be recognized in the upper right part of figure 6(*a*).

For comparison, figure 6(*b*) shows the result of the analogous experiment performed in a rectangular convection channel. This apparatus has no ramps: instead the upper and lower boundaries of the fluid are parallel over the entire length of the channel. The temperature difference again corresponds to a value of $\varepsilon = 0.03$. This large value without forcing the onset of nonlinear convection could only be achieved because an air bubble on the left-hand boundary prevents reflection there. The resistor for generating the heat pulses is located at $x = -10d$, outside the plotted region. Again, owing to the convective instability, the amplitude of the perturbation increases while travelling, and also the temporal broadening of the signal is present. Now, however, the wave reflected from the right-hand boundary is clearly evident in the upper left part of the picture.

### 4.3. *Reflection coefficient and the onset of the convective instability*

Rather than using the single perturbations shown in figure 6, for quantitative purposes it is more useful to generate heat pulses periodically in time. When stimulating the system with its Hopf frequency (one voltage pulse every 28.6 s), a periodic convection state will be achieved after some starting time with the entire accessible information contained in one period. In order to improve the signal-to-noise ratio, the profile lines obtained from many such periods (usually 300) are added together with the correct phase, leading to a time series of profile lines covering exactly one period and giving the intensity $I(x,t)$ as a function of space and time. Now for each spatial location $x$, the signal $I_x(t)$ can be transformed into Fourier space, thus yielding the strength $P^2$ of the mode with the stimulation period (which in principle is the only one occurring in the temporal spectrum) as a function of space. In figure 7(*a*), functions $P^2(x)$ measured in this way are shown for four different temperature differences and otherwise equal conditions. The lines correspond from top to bottom to $\Delta T = 10.60$, 10.54, 10.47 and 10.03 K. The resistor used for generating the heat pulses is located at $x \approx 7d$ causing the almost identical peaks there. Because of the ramp there is almost no propagation to the right, while the propagation to the left leads to different behaviours dependent on the respective temperature difference. After reaching a maximum inside the opposite ramp at $x \approx -5d$, the strength $P^2$ decreases strongly. The small periodic variations visible in the middle part contain the information about the reflected wave.

A theoretical expression for $P^2(x)$, valid for not too large convection amplitudes, can be modelled from the linear part of the amplitude equation (4.1) by superposing the left- and right-travelling waves and reintroducing the fast variations with $k_c$ and $\omega_c$ ($\varphi$ is a phase shift between the two waves; $A_0$ and $B_0$ are fixed by the selection of the coordinate system):

$$P^2(x) = A_0^2\, \mathrm{e}^{-\frac{2\varepsilon}{v_g\tau_0}x} + B_0^2\, \mathrm{e}^{\frac{2\varepsilon}{v_g\tau_0}x} + 2A_0B_0 \cos\left(2\left(k_c - \frac{\varepsilon c_0}{v_g\tau_0}\right)x + \varphi\right). \tag{4.5}$$

For our convection cell this result applies only inside the bulk regime between $x = \pm 3d$. By fitting this expression to the experimental data measured at various temperature differences, the values of $A_0$, $B_0$, $\varepsilon/v_g\tau_0$ and $k = k_c - (c_0\varepsilon/v_g\tau_0)$ can be extracted as functions of $\varepsilon$. An example for such a fit is shown by the line in figure 7(*b*), where the open circles represent the measurement points for a temperature difference of $\Delta T = 10.56$ K.

The results of those fits allow an accurate determination of the onset of the convective instability at $\Delta T_c^{con}$ by interpolating to that value of $\Delta T$ where $\varepsilon$ is zero. In that case, (4.5) reduces to $P^2(x, \varepsilon = 0) = A_0^2 + B_0^2 + 2A_0B_0\cos(2k_c + \varphi)$, which is constant except for the periodic variation with $2k_c$. From this procedure we obtain the value of $\Delta T_c^{con} = 10.03$ K (lowest line in figure 7*a*). Now the corresponding values of $\varepsilon$ can be calculated for all temperature differences $\Delta T$.

The values of $A_0$ and $B_0$ serve to deduce the reflection coefficient $r$. Because of the ramps, however, our convection channel has no well-defined lateral boundaries so that it is not quite clear where exactly the waves are reflected. Assuming this to occur at $x = x_r$, the reflection coefficient would be

$$r = \frac{B_0}{A_0}\, \mathrm{e}^{\frac{2\varepsilon}{v_g\tau_0}x_r}. \tag{4.6}$$

If $r$ is independent of $\varepsilon$, all functions $r(x) := (B_0/A_0)\exp(2\varepsilon x/v_g\tau_0)$ calculated for

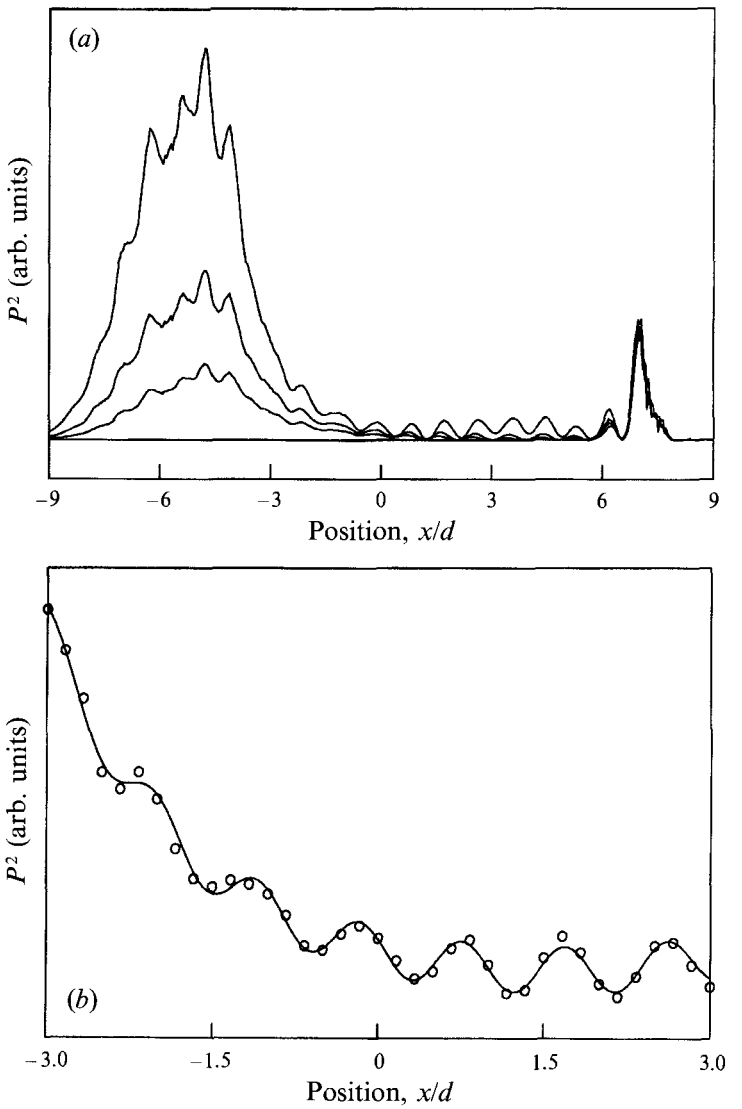


FIGURE 7. Analysis of the measurements using temporally periodic heat pulses to stimulate the system with its Hopf frequency $\omega_c$. For this purpose, every 28.6 s a short voltage pulse is applied to the resistor located at $x \approx 7d$ and the profile lines are recorded for exactly one period. (*a*) Strength $P^2$ of the mode showing the stimulation frequency as a function of the lateral position. From top to bottom the lines correspond to decreasing temperature differences: $\Delta T = 10.60$, 10.54, 10.47, and 10.03 K. (*b*) Example of a fit of the theoretical expression (4.5) for $P^2$ to the measurements shown in (*a*). The open circles are the measurement points and the line is the function fitted inside the bulk regime between $x = \pm 3d$. The temperature difference is $\Delta T = 10.56$ K.

different $\varepsilon$ should intersect in one point, namely at $x_r$. Five such curves $r(x)$ are drawn in figure 8(*a*) indeed showing the expected behaviour. From this plot the location of the reflection centre $x_r$ and the actual value of the reflection coefficient $r$ can be determined as

$$r \approx 0.006 \qquad \text{and} \qquad x_r \approx -6d. \tag{4.7}$$

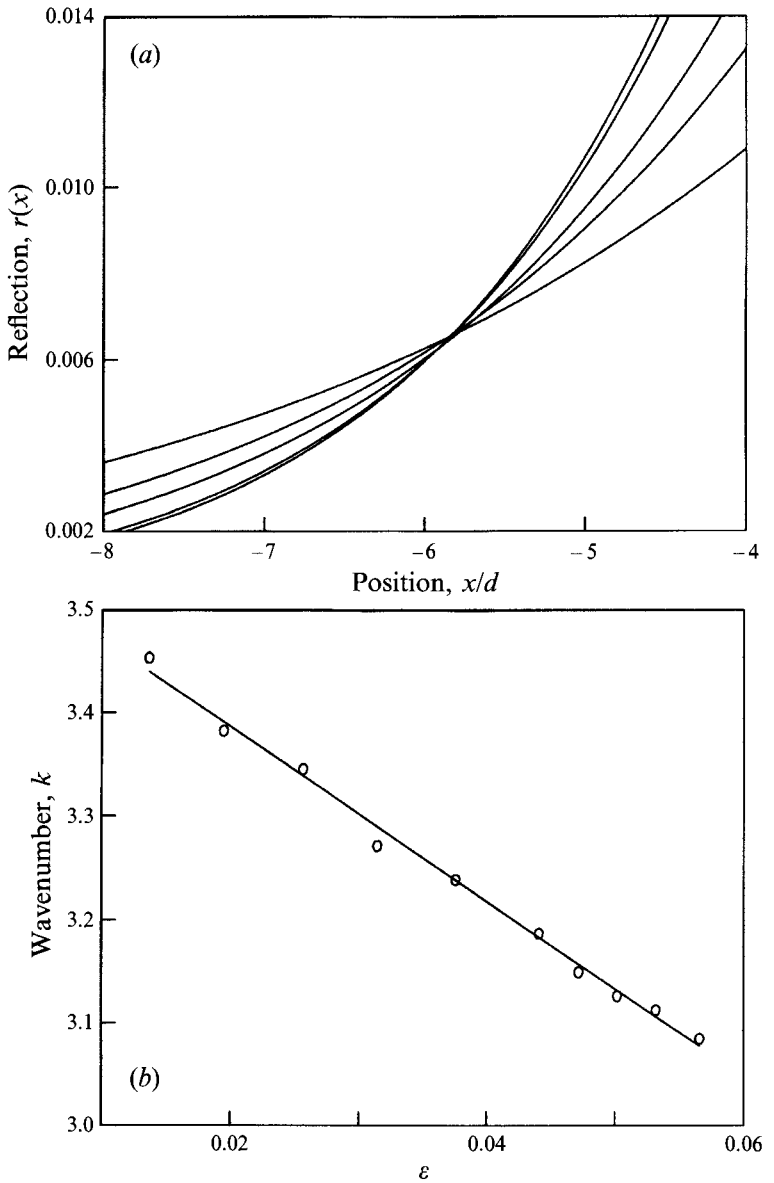


FIGURE 8. Results obtained from the periodic heat pulse measurements through fits analogous to that shown in figure 7(*b*). (*a*) The function $r(x) = (B_0/A_0)\exp(2\varepsilon x/v_g\tau_0)$ is plotted for different values of the temperature difference. The lines intersect at the centre of reflection at $x \approx -6d$ determining the reflection coefficient as $r \approx 0.006$. (*b*) The wavenumber as a function of $\varepsilon$ extracted from the measurements (open circles) can be modelled by the straight line obeying the law $k(\varepsilon) = k_c - (c_0\varepsilon/v_g\tau_0)$. This yields a critical wavenumber of $k_c = 3.56$ and $c_0/v_g\tau_0 = 8.46$.

At about 0.6 %, the reflection ability of our cell is considerably smaller than the usual values of 30–40 % (Cross 1986; Kolodner *et al.* 1987).

The open circles shown in figure 8(*b*) represent the wavenumbers obtained from these measurements for different temperature differences, and the straight line is a fit of the law $k = k_c - (c_0\varepsilon/v_g\tau_0)$ expected from (4.5), which obviously describes the

data quite well. This procedure determines the critical wavenumber as $k_c = 3.56$ and furthermore gives $c_0/v_g\tau_0 = 8.46$. From the results given in this section another two coefficients of the amplitude equation (4.1) can be calculated yielding $v_g\tau_0 = 0.16$ and $c_0 = 1.35$. Now the theoretical expression (4.3) for $\varepsilon_c^{ref}$ can also be tested and we find $\varepsilon_c^{ref} = 0.068$, which is in good agreement with the measured value of $\varepsilon_{c,exp}^{ref} = 0.06$, bearing in mind that (4.3) was an upper estimate.

## 5. Noise-induced convection structures

### 5.1. *Convection in the subcritical regime*

The amplification of travelling-wave states by the convective instability, as explained in detail in the last section, requires a more careful and quantitative investigation of the lower branch of figure 5 for $\Delta T < \Delta T_c^{ref}$. Here the system is not in a quiescent state without convection activity, as may be assumed in the first instance; instead, spontaneously occurring structures of extremely small amplitudes can be observed. Examples of such convective states are shown in figure 9 in the form of space–time plots. Here, the activity inside the spatial regime between $x = \pm 8d$ of the convection channel is represented for the duration of one hour. The temperature difference is $\Delta T = 10.42$ K ($\varepsilon = 0.039$) for the experiment shown in figure 9(*a*) and $\Delta T = 10.51$ K ($\varepsilon = 0.048$) in figure 9(*b*). For convenience the direction of the travelling waves is indicated by the arrows in the lower part of the pictures. During the times with higher convective activity in particular ('islands' of convection structures), the waves travelling to the right in the right part of the cell and to the left in the left part are quite distinct. Again the decrease of the amplitude inside the ramps forcing the waves to disappear is obvious. Rather than representing some part of a transient, these states are stable and can in principle be observed for an arbitrarily long time. Their amplitudes are so small that they could not be resolved against zero on the scale of figure 5.

At first sight the waves shown in figure 9 seem to originate in the middle of the convection channel, to travel subsequently towards the left- and right-hand boundaries. A more precise investigation, however, indicates that a wave observed for example in the right-hand part travelling to the right has made its way through the entire channel, but in the left-hand part it is usually hidden by left-travelling waves. This is caused by the amplification of the waves during their travel due to the convective nature of the instability, resulting in the structures being much better detected in their destination part of the cell. In fact, the high quality of the quantitative analysis presented in §§ 5.2 and 5.3 is only made possible by this intrinsic amplification mechanism. From figure 9 some alterations of the convection behaviour with varying temperature difference can be recognized at least qualitatively. At the higher temperature difference, the 'islands' of travelling-wave activity persist for a longer time, so obviously the correlation time increases. Also the mean amplitude of the structures increases with increasing temperature difference leading to a better contrast against the background.

Each of the profile lines shown in figure 9 is obtained by adding together the intensities of all the lines covering the vertical dimension of the convection channel (about 70 lines). Typical values for the variations of the light intensities (in units of grey scales of our camera) are $\Delta I \approx 1.5$ for figure 9(*a*) and $\Delta I \approx 4.8$ for figure 9(*b*) at an average intensity of $I \approx 2500$ for the incoming light beam. The smallest still measurable convection structures observed at $\varepsilon = -0.02$ yield $\Delta I \approx 0.5$ (these

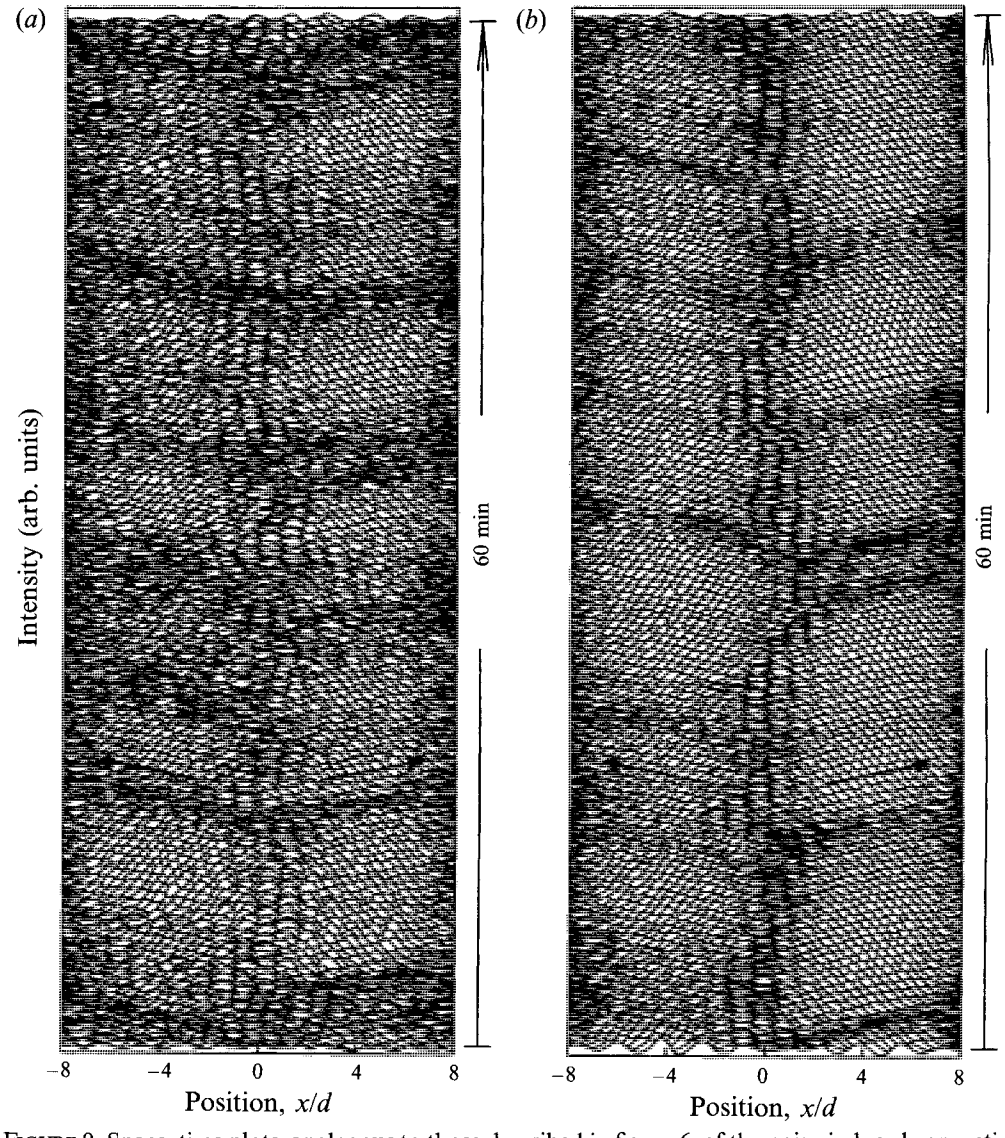


FIGURE 9. Space–time plots, analogous to those described in figure 6, of the noise-induced convection structures. Linear waves with very small amplitudes can be recognized travelling to the right in the right-hand part of the channel and to the left in the left-hand part to eventually vanish inside the ramps. The direction of propagation is indicated by the arrows in the lower part of the pictures. The patches of higher convective activity occur randomly in time. Their duration and thus correlation and also their mean amplitude increase with increasing temperature difference. These states are discussed in detail in the text. (*a*) $\Delta T = 10.42$ K ($\varepsilon = 0.039$), (*b*) $\Delta T = 10.51$ K ($\varepsilon = 0.048$).

structures could no longer be made visible in the form of a plot analogous to figure 9). Hence when taking only one profile line for example in the middle of the convection channel, information about the convection patterns was hidden in 0.01 to 0.1 of one grey-scale level of the CCD–camera. To observe and analyse these structures, various digital methods for improving the signal-to-noise ratio must be used, the simplest one being integration over the entire vertical extent of the cell. Moreover, six such profile lines were added together for each measurement point in time rather than just one.

For presenting the images in the form of the plots shown in figure 9, the data have been additionally filtered spatially and temporally.

### 5.2. *Quantitative analysis of the convection structures*

As mentioned earlier only three pairs of convection rolls fit into the bulk part, leading to a poor spatial resolution. Therefore the quantitative analysis of the noise-induced structures is performed exclusively in the time regime. Here, on the other hand, the measurements are very precise, because the structures can in principle be observed for an arbitrarily long time. Figure 10 shows the observed light intensity as a function of time for 8192 s at one spatial location on the right-hand side of the bulk part of the channel ($x = 3d$, lower half) and at one location on the left-hand side ($x = -3d$, upper half). The applied temperature difference is $\Delta T = 10.54$ K corresponding to $\varepsilon = 0.051$. The fast variation of the waves with the Hopf frequency can no longer be resolved on this scale, so that figure 10 is a representation of the envelope of 'islands' of convection structures as shown in figure 9. These 'islands' showing higher convection activity arise randomly with variable length, but nevertheless they obviously have a well-defined mean duration, which grows longer with increasing temperature difference. The behaviour in one half of the channel seems not to be coupled to that in the other half. The scenario is qualitatively the same over the entire range of existence of these states and also remains stationary for long observation times. The measurement points were chosen to be at the boundaries of the bulk regime at $x = \pm 3d$, because here the maximal amplification of the waves due to the convective instability can be expected.

An appropriate tool for investigating such stochastic structures is the temporal correlation function (here for the measured light intensity) given by

$$f_{cor}(I, \Delta t) = \frac{1}{T} \int_0^T I(t) I(t + \Delta t)\, \mathrm{d}t. \tag{5.1a}$$

Usually more convenient for the analysis of experimental data, however, is the structure function (see e.g. Schulz-DuBois & Rehberg 1981)

$$f_{sfu}(I, \Delta t) = \frac{1}{T} \int_0^T \big(I(t) - I(t + \Delta t)\big)^2\, \mathrm{d}t. \tag{5.1b}$$

If a statistically stationary process is considered and the observation time is 'long enough', the latter is related to the correlation function via $f_{sfu}(I, \Delta t) = \text{const.} - 2 f_{cor}(I, \Delta t)$, so that the correlation function can easily be determined from the structure function.

For the quantitative analysis of the observed convection structures, time series such as shown in figure 9 were taken for various temperature differences between $\Delta T_s = 9.61$ K and $\Delta T_c^{ref} = 10.61$ K. Each measurement consists of 2048 profile lines, one taken every 2 s. Each single profile line represents a sum of six lines, which are again all integrated over the whole vertical dimension of the channel. For further improvement of the signal-to-noise ratio, the structure function was not only calculated for just one location, but for 32 neighbouring pixels on the right-hand side of the channel and for 32 on the left-hand side, which are eventually all added together. The temporal correlation functions obtained in this way are shown by the closed squares in figure 11 for three different temperature differences (the lines are fits of (5.2) and are discussed in § 5.3). The correlation functions are normalized to their respective value at $\Delta t = 0$ and the temperature difference is from top to bottom $\Delta T = 10.58$ K ($\varepsilon = 0.055$), $\Delta T = 10.24$ K ($\varepsilon = 0.021$) and $\Delta T = 10.06$ K

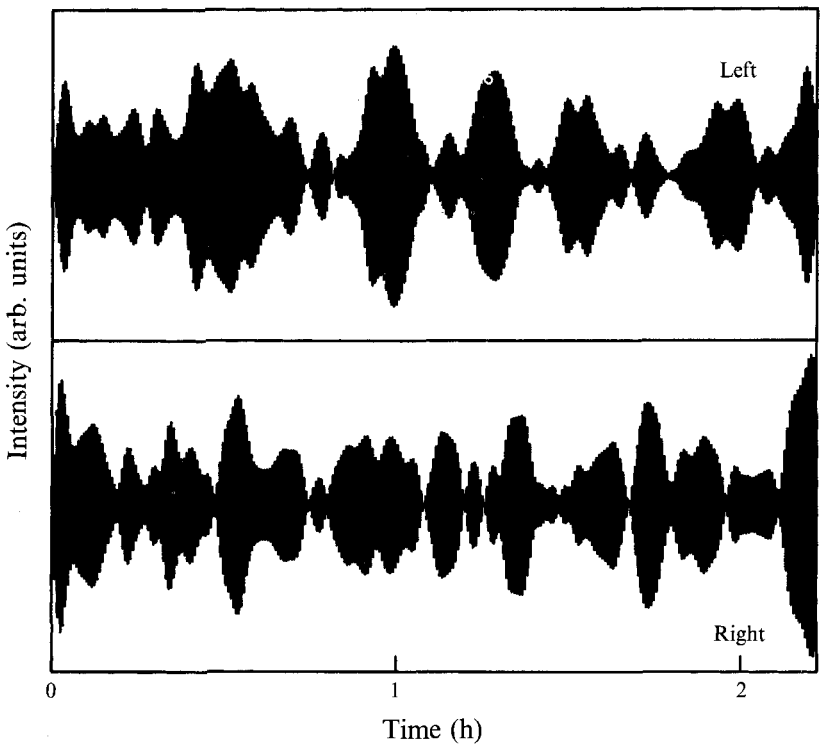


FIGURE 10. Envelope of noise-induced convection structures, similar to those plotted in figure 9, for $\Delta T = 10.54$ K ($\varepsilon = 0.051$). The light intensity taken from the shadowgraph image is shown as a function of time for 8192 s for one location at the left-hand ($x = -3d$, upper part) and for one location at the right-hand ($x = +3d$, lower part) boundary of the bulk regime, respectively. The randomly occurring patches of higher convective activity as discussed for figure 9 are well pronounced. The fast variation with the Hopf frequency cannot be resolved on this scale.

($\varepsilon = 0.003$). The Hopf frequency of the travelling waves can clearly be seen, especially for the upper two measurements. When decreasing the temperature difference, the correlation function becomes noisier and decays faster, but some useful information can be extracted even from figure 11(*c*).

### 5.3. *Comparison with the theory*

A theory which takes into account the influence of thermal noise on the convection onset in a spatially extended system was recently presented for the case of binary fluid mixtures with realistic boundary conditions by Schöpf & Zimmermann (1993) following the classic work of Graham (1974), which was valid for normal one-component fluids between free-slip boundaries. The idea and results of this theory were briefly outlined and summarized in § 2. This theory should describe our measurements if the observed convection structures are indeed noise-induced, although the noise need not necessarily be thermal as long as the $\delta$-correlations given in (2.2*a–c*) are correct. Since we are dealing with very small convection amplitudes, the spatio-temporal correlation function (2.6), which could be deduced from the amplitude equation (2.4) by neglecting the nonlinear terms, is considered to be sufficient in our case. For our analysis in the form of purely temporal correlation functions measured at a fixed position, we have $\Delta x = 0$ in (2.6). If we additionally neglect in the first instance $c_1 = 0.09$ compared with 1, leading to $\bar{c}_1 = 1$, the experimental analysis of this expression is

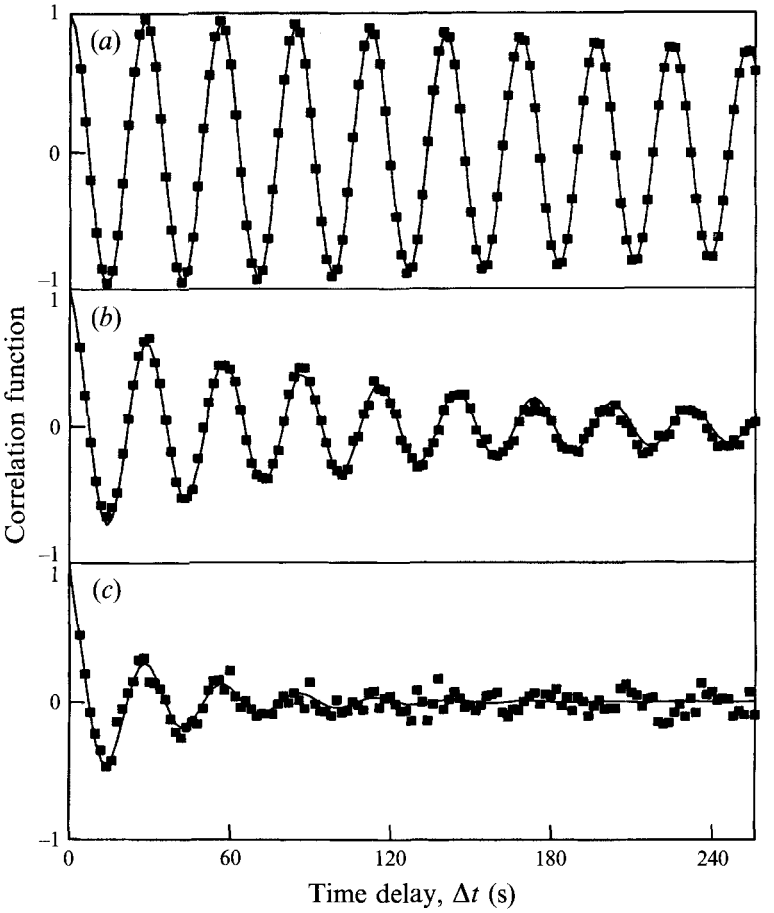


FIGURE 11. Temporal autocorrelation functions of the noise-induced convection structures. These functions are obtained from measurements similar to those shown in figure 9. From the profile lines taken every 2 s for 4096 s altogether, the functions are calculated at 64 fixed locations around $x = \pm 3d$ and then added together, yielding the measurement points represented by the closed squares. The lines are fits of (5.2), which obviously describes the experiments quite well. The functions are normalized to their maximal values at $\Delta t = 0$ and are calculated for time delays up to $\Delta t = 256$ s. The temperature differences are (*a*) $\Delta T = 10.58$ K ($\varepsilon = 0.055$), (*b*) $\Delta T = 10.24$ K ($\varepsilon = 0.021$), (*c*) $\Delta T = 10.06$ K ($\varepsilon = 0.003$).

further simplified without losing essential information. The analytical expression for the temporal correlation function of the light intensity is then given by

$$f_{cor}(I, \Delta t) = \tfrac{1}{2}\hat{I}^2 \left\{ \mathrm{e}^{-\frac{\Delta t}{t_1}} \operatorname{erfc}\left( \left(\frac{\Delta t}{t_0}\right)^{\frac{1}{2}} - \tfrac{1}{2}\left(\frac{t_0 \Delta t}{t_1^2}\right)^{\frac{1}{2}} \right) \right.$$
$$\left. + \mathrm{e}^{+\frac{\Delta t}{t_1}} \operatorname{erfc}\left( \left(\frac{\Delta t}{t_0}\right)^{\frac{1}{2}} + \tfrac{1}{2}\left(\frac{t_0 \Delta t}{t_1^2}\right)^{\frac{1}{2}} \right) \right\} \cos(\omega \Delta t). \qquad (5.2)$$

The fast variation with the Hopf frequency has to be reintroduced to take care of the rapid oscillation observed in the experimental system (Schöpf & Zimmermann 1993; actually the amplitude equation (2.4) describes the deviations from this fast oscillation). This result can be fitted to the measurement points, and is represented

by the lines shown in figure 11 and thus obviously describes the experimental date quite well. For a real quantitative interpretation, however, the dependence of the parameters of (5.2) on the control parameter $\varepsilon$ has to be examined. From the fits, we obtain besides the frequency $\omega$ the mean intensity variation $\hat{I}$ and the two correlation times $t_0$ and $t_1$, the latter three being expected to diverge at the critical point where they obey different laws (Schöpf & Zimmermann 1993). It is known from finite systems undergoing a Hopf bifurcation that owing to the non-perfect reflection of the travelling waves from the sidewalls the onset of nonlinear convection occurs at $\varepsilon_c^{ref}$ (see also § 4). Therefore the shifted control parameter $\bar{\varepsilon} = (\Delta T - \Delta T_c^{ref})/\Delta T_c^{ref}$ has to be used for analysing the scaling laws. In our experiment the divergence point for the parameters of interest is indeed given by this reflection-induced onset of nonlinear convection (see figure 12).

Fitting (5.2) to the obtained correlation functions analogously to figure 11 for all the measurements, the important parameters can be extracted as functions of the temperature difference. These parameters are shown in figure 12 and will now be discussed in turn. The open squares correspond to increasing and the closed circles to decreasing $\Delta T$, hence no hysteresis effects are present. The small arrows inside the lower two pictures indicate the onset of the convective instability at $\Delta T = 10.03$ K ($\varepsilon = 0$).

Figures 12(*a*) and 12(*b*) show the correlation times $t_0$ and $t_1$, which measure the decay of a spatially uniform and a spatially modulated state, respectively. For too small temperature differences, the uncertainties become so large that the data no longer make a meaningful contribution (see e.g. figure 11*c*) and are therefore not shown. The lines are fits of the expected laws (Schöpf & Zimmermann 1993)

$$t_0 = \frac{\tau_0}{-\bar{\varepsilon}} \qquad \text{and} \qquad t_1 = \frac{\xi_0}{v_g(-\bar{\varepsilon})^{\frac{1}{2}}} \tag{5.3}$$

and obviously describe the data quite well yielding $\tau_0 \approx 47$ s and $\xi_0/v_g \approx 23$ s. It should be mentioned that a simple single-mode model as discussed in § 6, by (6.1) only involves one decay time $t_0$, which moreover is not compatible with the respective decay law.

The frequency $\omega$ shown in figure 12(*c*) can be determined very well especially for large $\Delta T$ (see e.g. figure 11*a*, *b*). For smaller temperature differences, the correlation functions are noisier (see e.g. the lowest picture of figure 11) leading to a larger scatter for the extracted frequency. The slight increase with $\Delta T$ can be understood from a linear analysis of the amplitude equation (4.1).

With help of (3.6) the intensity variation $\hat{I}$ obtained from these procedures can now be converted into the temperature variation via $\hat{T}_{exp} \approx (\hat{I}/2500)\,0.64$ K, which is shown by the symbols in figure 12(*d*). Following Schöpf & Zimmermann (1993), this should be described by $\hat{T}_{exp} = \hat{T}_0/(-\bar{\varepsilon})^{\frac{1}{4}}$. However, it has to be taken into account that the measured structures are already amplified by the convective instability, hence this $\hat{T}_{exp}$ is not the strength of the basic fluctuations that have induced the convection structures. Rather an amplification factor has to be considered when comparing the experimental data with the theory, yielding

$$\hat{T}_{exp} = \frac{\hat{T}_0}{(-\bar{\varepsilon})^{\frac{1}{4}}}\, \mathrm{e}^{\frac{x_m}{\tau_0 v_g}\varepsilon} \tag{5.4a}$$

with

$$\varepsilon = \frac{\Delta T - \Delta T_c^{con}}{\Delta T_c^{con}} \qquad \text{and} \qquad \bar{\varepsilon} = \frac{\Delta T - \Delta T_c^{ref}}{\Delta T_c^{ref}} \tag{5.4b}$$

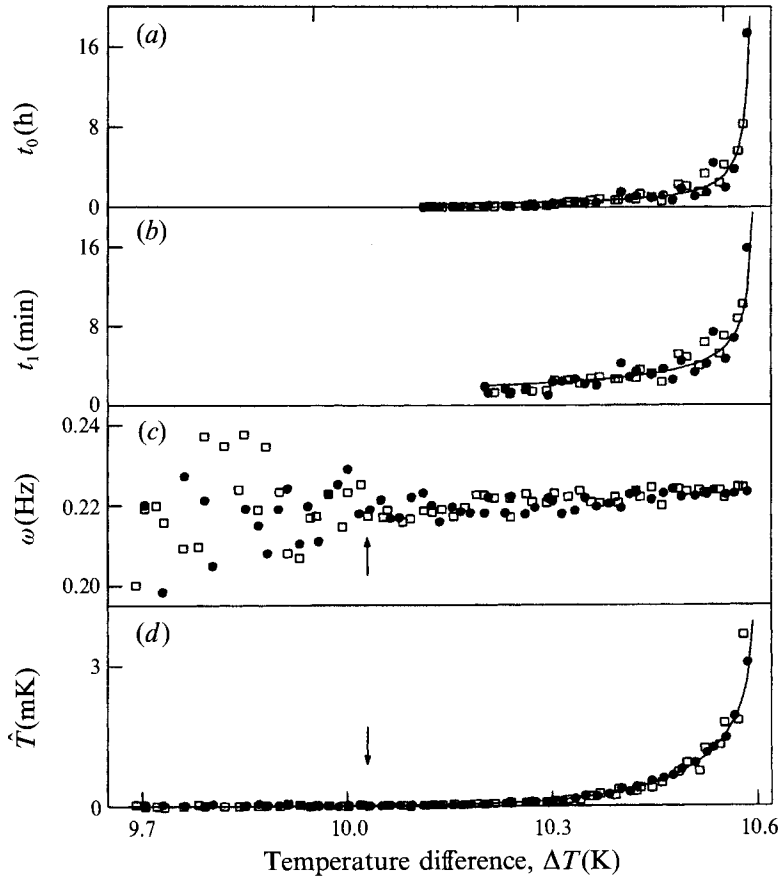


FIGURE 12. Final results for the noise-induced convection structures. The parameters are obtained from fits of (5.2) to the measured correlation function similar to those shown in figure 11. The respective values are given as functions of the applied temperature difference $\Delta T$ for increasing (open squares) and for decreasing (closed circles) $\Delta T$. The lines are fits of the theoretically expected scaling laws. The small arrow in the lower two pictures indicates the onset of the convective instability at $\Delta T = 10.03$ K ($\varepsilon = 0$). (*a*) Correlation time $t_0$, (*b*) correlation time $t_1$, (*c*) frequency $\omega$, (*d*) mean temperature variation $\hat{T}$.

as the correct law. $x_m$ is the average distance between the origin of the convective structures and the measurement point and $\hat{T}_0$ is the noise strength that is responsible. The fit of (5.4*a*) to the experimental data is represented by the line in figure 12(*d*), which without the inclusion of the $\varepsilon$-dependent amplification factor would not describe the data correctly. Also the law $\hat{T}_{exp} \propto (-\varepsilon)^{-\frac{1}{2}}$ following from the single-mode model discussed by (6.1) below is not sufficient. For the fit of (5.4), a constant offset is included in order to account for systematical errors. The best agreement with the theoretical model is achieved for a value of about 0.12 mK for this offset, while the values of $\Delta T_c^{con}$ and $\Delta T_c^{ref}$ are kept fixed to 10.03 and 10.60 K, respectively. This procedure finally gives $x_m = (12.8 \pm 0.5)\, d$, thus indicating that the fluctuations responsible for our measurements originate somewhere inside the opposite ramp. For the experimental noise strength we find

$$\hat{T}_{0,exp} \approx (6.3 \pm 0.9) \times 10^{-6}\ \text{K}. \tag{5.5a}$$

This value can be calculated theoretically from the fundamental hydrodynamic equations, when the noise is assumed to be due to thermal fluctuations (Schöpf & Zimmermann 1993). Doing this analogously to our experiment as the average over the entire vertical dimension of the convection cell, we get

$$\hat{T}_{0,theo} = 5.3 \times 10^{-6}\ \mathrm{K}. \tag{5.5b}$$

Taking into account the extremely small convection amplitudes giving rise to the experimental difficulties described, this can be considered as a very good agreement. Hence the observed convection structures can be interpreted as the manifestation of thermal noise.

It is very remarkable that the measured fluctuations can be explained in terms of the intrinsic thermal noise alone, without assuming any additional noise sources. This indicates that the external fluctuations of the control parameter as shown in figure 2(*c*) are not effective in producing convection patterns. An explanation of this finding might be the fact that these fluctuations have a very long wavelength, which is given by the order of the length of the convection channel. They are thus inefficient in producing convection rolls, which have a much shorter wavelength.

## 6. Discussion

The experiments described in this paper make use of the convective instability which arises as a consequence of the Hopf bifurcation occurring in binary fluid mixtures for negative separation ratios. With the help of a specially designed convection channel, the reflection of the travelling waves from the sidewalls could be drastically reduced, so that the onset of nonlinear convection was shifted by a relative amount of the control parameter of about 6%. Therefore, homogeneous disturbances could not trigger the convection onset before the positive value of $\varepsilon = 0.058$ is reached, thus opening a relatively large range of the convective instability, inside which linear features of the system can be investigated. The reflection behaviour was identified by stimulating the system from outside with its own Hopf frequency, a procedure which additionally yields some of the linear coefficients of the amplitude equation being used to describe the convection near onset. These coefficients deviate to some extent from the values calculated directly from the basic hydrodynamic equations. The calculations, however, were performed for a two-dimensional infinitely extended system. For narrow systems like the quasi-one-dimensional convection apparatus used in our experiment, such calculations have not been carried out yet.

The main results of our measurements are extracted from the behaviour of the convection patterns with extremely small amplitudes found in the subcritical range. Besides a good thermal insulation of the experimental apparatus and a very high sensitivity of the shadowgraph method used for quantifying the convection structures, the investigation of these patterns was made possible mainly by the intrinsic amplification of the structures due to the convective instability. For the data obtained at temperature differences near $\varepsilon_c^{ref}$, which are most responsible for the determination of the noise strength, the amplification factor reached values between 20 and 100. The strength of the perturbations triggering the convective structures is in very good agreement with theoretical predictions if thermal noise is assumed to be the reason for the disturbances. However, a critical discussion of different interpretations seems to be appropriate.

At first sight, these states may be assumed to be related to the formerly observed 'blinking states' (see e.g. Fineberg, Moses & Steinberg 1988; Kolodner & Surko 1988;

Steinberg *et al.* 1989). The latter can be explained theoretically by the interaction and superposition of travelling waves reflected from the boundaries using coupled amplitude equations (Cross 1986, 1988). In our experiment, however, nonlinear interactions are unlikely to have a measurable influence because of the extremely small convection amplitudes. As discussed in §4, reflection should also not play any significant role. Moreover the theoretical analysis as well as the experimental observations of the 'blinking states' indicate a qualitatively different scenario when changing the temperature difference. This is definitely not the case in our experiment, where the erratic character shown in figure 9 persists over the entire range of $\Delta\varepsilon \approx 0.08$, where these structures could be observed. An explanation in the form of 'blinking states' can therefore be excluded.

For similar reasons, we do not think that our results can be explained in terms of the 'dispersive chaos' found by Kolodner *et al.* (1990) in an annular convection apparatus for much smaller values of $|\psi|$. This scenario is an interplay of convectively amplified small structures, which finally break down and decay owing to nonlinear dispersion. This latter part has never been observed in our experiments, where rather the waves decay owing to the presence of the ramps. Again we want to emphasize that we found no hint of a nonlinear behaviour. According to the results given by Kolodner *et al.* (1990), the characteristics of the 'dispersive chaos' change qualitatively with varying the temperature difference, a fact which is dissimilar to our experiment. Also, those authors did not find these states for $\psi \leqslant -0.05$.

As another possibility for the theoretical modelling, a simpler decay law for the correlation function in the form of

$$f_{cor}(I, \Delta t) = \hat{I}^2 \mathrm{e}^{-\frac{\Delta t}{t_0}} \cos(\omega \Delta t) \tag{6.1}$$

could be assumed in the first instance, guided by the measurements (see figure 11). This law can indeed be derived from a theory involving a noise term, when no spatial variations are considered, i.e. from a single-mode model like for example (2.4) without spatial derivatives. Equation (6.1) could also describe the measurements shown in figure 11, yielding information about the average light intensity $\hat{I}$, the frequency $\omega$ and the decay time $t_0$. For this model, the intensity should vary like $\hat{I} \propto (-\varepsilon)^{-\frac{1}{2}}$ and the decay time like $t_0 \propto (-\varepsilon)^{-1}$; however, neither of these is compatible with the experimental data. Hence, even if this simple model could be used to determine correctly the frequency and the amplitude of the structure, it is not sufficent to explain our experiment. The more sophisticated theory leading to the expression (5.2) for the correlation function, on the other hand, not only describes the experiments quite well, but also shows the correct behaviour of the extracted experimental parameters.

At this point we would like to correct some errors occurring in our preceding paper, where some of the results have been briefly presented (Schöpf & Rehberg 1992). Although the main conclusions are correct, the presentation, especially of figure 5 there, could give rise to some confusion. The theory on this topic has also been improved in the meantime. The fluid mixture was claimed to consist of 16.98 % ethanol, while the correct value is 22.04 % corresponding to $L = 0.009$, $Pr = 15.5$ and $\psi = -0.125$. These parameters were determined using a program which meanwhile was kindly made available by P. Kolodner (see also Kolodner *et al.* 1988). For calculating the correlation times, a factor of 2 was overlooked, so that the results for $t_0$ and $t_1$ given by Schöpf & Rehberg (1992) have to be multiplied by 2 (also in figure 5 therein). Also in figure 5, rather than $\omega$, $f = \omega/2\pi$ was shown. Finally, instead of $\hat{T}$ the value $4\tau_0\xi_0\hat{T}$ was plotted, where moreover the change of the refractive index

due to the concentration variation has not been taken into account (see § 3.2). For comparison with theory, calculations valid for free permeable boundary conditions were cited, while the results for realistic boundaries now exist.

In summary, we have measured hydrodynamic fluctuations of thermal origin by using the convective instability, which was treated by a somewhat simplified procedure in the theoretical analysis. A more detailed theoretical modelling of our data is currently in progress (private communication by G. Ahlers). The measurements shown in figure 11 suggest that a direct observation without the use of an intrinsic amplification should also be possible below $\varepsilon = 0$, if a convection cell of smaller height is used. In this connection it is worth pointing out that a direct observation of such thermal fluctuations seems also possible in Rayleigh–Bénard convection in a gas (see Bodenschatz *et al.* 1992). Moreover, the possibility of measuring the influence of thermal noise on Taylor vortices is currently under investigation (Babcock, Ahlers & Cannell 1991; Tsameret & Steinberg 1991; Babcock, Cannell & Ahlers 1992). Thus, hydrodynamic fluctuations may become observable for a growing number of hydrodynamic instabilities, which gives rise to the hope that even the theoretical ideas concerning the nonlinear interaction of these fluctuations might be tested experimentally in the near future.

We would like to thank G. Ahlers, H. R. Brand, P. Kolodner, M. Lücke, V. Steinberg and especially L. Kramer for many discussions and stimulating criticism. The experiments were supported by Stiftung Volkswagenwerk and by a NATO Collaborative Research Grant 910112.

## REFERENCES

AHLERS, G., CROSS, M. C., HOHENBERG, P. C. & SAFRAN, S. 1981 *J. Fluid Mech.* **110**, 297.

AKHIEZER, A. I. & POLOVIN, R. V. 1971 *Usp. Fiz. Nauk* **104**, 185 [1971 *Sov. Phys. Uspekhi* **14**, 278].

BABCOCK, K. L., AHLERS, G. & CANNELL, D. S. 1991 *Phys. Rev. Lett.* **67**, 3388.

BABCOCK, K. L., CANNELL, D. S. & AHLERS, G. 1992 *Physica* D **61**, 40.

BARTEN, W., LÜCKE, M., HORT, W. & KAMPS, M. 1989 *Phys. Rev. Lett.* **63**, 376.

BÉNARD, H. 1900 *Revue Gén. Sci. Pures et Appl.* **11**, 1261 and 1309.

BENSIMON, D., KOLODNER, P., SURKO, C. M., WILLIAMS, H. & CROQUETTE, V. 1990 *J. Fluid Mech.* **217**, 441.

BODENSCHATZ, E., MORRIS, S. W., BRUYN, J. R. DE, AHLERS, G. & CANNELL, D. S. 1992 In *The Physics of Pattern Formation in Complex Dissipative Systems* (ed. S. Kai), p. 227. World Scientific.

BODENSCHATZ, E., ZIMMERMANN, W. & KRAMER, L. 1988 *J. Phys. (Paris)* **49**, 1875.

BRAND, H. R., HOHENBERG, P. C. & STEINBERG, V. 1984 *Phys. Rev.* A **30**, 2548.

BRAND, H. R., LOMDAHL, P. S. & NEWELL, A. C. 1986 *Physica* **23**D, 345.

BRAND, H. R. & STEINBERG, V. 1983 *Physica* **119**A, 327.

BRETHERTON, C. S. & SPIEGEL, E. A. 1983 *Phys. Lett.* **96**A, 152.

BRIGGS, R. J. 1964 *Electron–Stream Interaction with Plasmas.* Research Monograph No. 29. MIT Press.

BUSSE, F. H. & KRAMER, L. (ed.) 1990 *Nonlinear Evolution of Spatio-Temporal Structures in Dissipative Continuous Systems.* Plenum.

BUSSE, F. H. & WHITEHEAD, J. A. 1971 *J. Fluid Mech.* **47**, 305.

BUSSE, F. H. & WHITEHEAD, J. A. 1974 *J. Fluid Mech.* **66**, 67.

CHANDRASEKHAR, S. 1961 *Hydrodynamic and Hydromagnetic Stability.* Oxford University Press.

CHOCK, D. P. & LI, C. 1975 *Phys. Fluids* **18**, 1401.

COULLET, P. & HUERRE, P. (ed.) 1990 *New Trends in Nonlinear Dynamics and Pattern-Forming Phenomena: The Geometry of Nonequilibrium.* Plenum.

COULLET, P. H. & SPIEGEL, E. A. 1983 *SIAM J. Appl. Maths* **43**, 776.

CROQUETTE, V. & WILLIAMS, H. 1989 *Physica* D **37**, 300.

Cross, M. C. 1986 *Phys. Rev. Lett.* **57**, 2935.
Cross, M. C. 1988 *Phys. Rev.* A **38**, 3593.
Cross, M. C. & Kim, K. 1988 *Phys. Rev.* A **37**, 3909.
Deissler, R. J. 1985 *J. Statist. Phys.* **40**, 371.
DiPrima, R. C. & Swinney, H. L. 1981 In *Hydrodynamical Instabilities and the Transition to Turbulence* (ed. H. L. Swinney & J. P. Gollub), p. 139. Springer.
Fineberg, J., Moses, E. & Steinberg, V. 1988 *Phys. Rev. Lett.* **61**, 838.
Frick, H. & Clever, R. M. 1980 *Z. Angew. Math. Phys.* **31**, 502.
Gershuni, G. Z. & Zhukhovitskii, E. M. 1976 *Convective Stability of Incompressible Fluids*. Keter.
Graham, R. 1974 *Phys. Rev.* A **10**, 1762.
Graham, R. & Pleiner, H. 1975 *Phys. Fluids* **18**, 130.
Heutmaker, M. S., Fraenkel, P. N. & Gollub, J. P. 1985 *Phys. Rev. Lett.* **54**, 1369.
Hohenberg, P. C. & Swift, J. 1992 *Phys. Rev.* A **46**, 4773.
Huerre, P. & Monkewitz, P. A. 1985 *J. Fluid Mech.* **159**, 151.
Hurle, D. T. J. & Jakeman, E. 1971 *J. Fluid Mech.* **47**, 667.
Khalatnikov, I. M. 1957 *Zh. Exsp. Teor. Fiz.* **33**, 809 [1957 *Sov. Phys. JETP* **6**, 624].
Knobloch, E. 1986 *Phys. Rev.* A **34**, 1538.
Knobloch, E. & Moore, D. R. 1988 *Phys. Rev.* A **37**, 860.
Knobloch, E. & Proctor, M. R. E. 1981 *J. Fluid Mech.* **108**, 291.
Kolodner, P. 1993 *Phys. Rev.* E **48**, 4187.
Kolodner, P., Glazier, J. A. & Williams, H. 1990 *Phys. Rev. Lett.* **65**, 1579.
Kolodner, P., Passner, A., Surko, C. M. & Walden, R. W. 1986*a* *Phys. Rev. Lett.* **56**, 2621.
Kolodner, P. & Surko, C. M. 1988 *Phys. Rev. Lett.* **61**, 842.
Kolodner, P., Surko, C. M., Passner, A. & Williams, H. L. 1987 *Phys. Rev.* A **36**, 2499.
Kolodner, P., Walden, R. W., Passner, A. & Surko, C. M. 1986*b* *J. Fluid Mech.* **163**, 195.
Kolodner, P., Williams, H. & Moe, C. 1988 *J. Chem. Phys.* **88**, 6512.
Landau, L. D. & Lifshitz, E. M. 1957 *Zh. Exsp. Teor. Fiz.* **32**, 618 [1957 *Sov. Phys. JETP* **5**, 512].
Landau, L. D. & Lifshitz, E. M. 1959 *Fluid Mechanics*. Pergamon.
Lee, G. W. T., Lucas, P. & Tyler, A. 1983 *J. Fluid Mech.* **135**, 235.
Legros, J. C., Longree, D., Chavepeyer, G. & Patten, J. K. 1975 *Physica* **80**A, 76.
Lekkerkerker, H. N. W. 1975 In *Fluctuations, Instabilities and Phase Transitions* (ed. T. Riste), p. 189. Plenum Press.
Lekkerkerker, H. N. W. & Laidlaw, W. G. 1977 *J. Phys. (Paris)* **38**, 1.
Lhost, O. & Platten, J. K. 1988 *Phys. Rev.* A **38**, 3147.
Lhost, O. & Platten, J. K. 1989 *Phys. Rev.* A **40**, 6415.
Linz, S. J. & Lücke, M. 1987 *Phys. Rev.* A **35**, 3997.
Lusty, M. E. & Dunn, M. H. 1987 *Appl. Phys.* B **44**, 193.
Meyer, C. W., Ahlers, G. & Cannell, D. S. 1991 *Phys. Rev.* A **44**, 2514.
Moses, E. & Steinberg, V. 1986 *Phys. Rev.* A **34**, 693.
Newell, A. C. 1974 *Lect. Appl. Math.* **15**, 157.
Newell, A. C. & Whitehead, J. 1969 *J. Fluid Mech.* **38**, 279.
Nield, D. A. 1967 *J. Fluid Mech.* **29**, 545.
Pedersen, A. M. & Riste, T. 1980 *Z. Phys.* B **37**, 171.
Platten, J. K. & Legros, L. C. 1984 *Convection in Liquids*. Springer.
Rasenat, S., Hartung, G., Winkler, B. L. & Rehberg, I. 1989 *Exp. Fluids* **7**, 412.
Rayleigh, Lord 1916 *Phil. Mag.* **32**, 529.
Rehberg, I. & Ahlers, G. 1985 *Phys. Rev. Lett.* **55**, 500.
Rehberg, I., Hörner, F., Chiran, L., Richter, H. & Winkler, B. L. 1991*a* *Phys. Rev.* A **44**, 7885.
Rehberg, I., Rasenat, S., Torre Juárez, M. de la, Schöpf, W., Hörner, F., Ahlers, G. & Brand, H. R. 1991*b* *Phys. Rev. Lett.* **67**, 596.
Rehberg, I., Winkler, B. L., Torre Juárez, M. de la, Rasenat, S. & Schöpf, W. 1989 *Festkörperprobleme* **29**, 35.
Saarlos, W. van & Hohenberg, P. C. 1990 *Phys. Rev. Lett.* **64**, 749.
Schöpf, W. 1992 *J. Fluid Mech.* **245**, 263.

SCHÖPF, W. & KRAMER, L. 1991 *Phys. Rev. Lett.* **66**, 2316.

SCHÖPF, W. & REHBERG, I. 1992 *Europhys. Lett.* **17**, 321.

SCHÖPF, W. & ZIMMERMANN, W. 1989 *Europhys. Lett.* **8**, 41.

SCHÖPF, W. & ZIMMERMANN, W. 1990 *Phys. Rev.* A **41**, 1145.

SCHÖPF, W. & ZIMMERMANN, W. 1993 *Phys. Rev.* E **47**, 1739.

SCHULZ-DUBOIS, E. O. & REHBERG, I. 1981 *Appl. Phys.* **24**, 323.

SMITH, I. W., GALERNE, Y., LAGERWALL, S. T., DUBOIS-VIOLETTE, E. & DURAND, G. 1975 *J. Phys. Coll.* C **1**, 237.

STANLEY, H. E. 1971 *Introduction to Phase Transitions and Critical Phenomena.* Oxford University Press.

STEINBERG, V., AHLERS G. & CANNELL, D. S. 1985 *Physica Scripta* T **9**, 97.

STEINBERG, V., FINEBERG, J., MOSES, E. & REHBERG, I. 1989 *Physica* D **37**, 359.

STEWARTSON, J. & STEWART, J. T. 1971 *J. Fluid Mech.* **48**, 529.

SULLIVAN, T. S. & AHLERS, G. 1988 *Phys. Rev. Lett.* **61**, 78.

SWIFT, J. & HOHENBERG, P. C. 1977 *Phys. Rev.* A **15**, 319.

SWINNEY, H. L. & GOLLUB, J. P. (ed.) 1981 *Hydrodynamical Instabilities and the Transition to Turbulence.* Springer.

TAYLOR, G. I. 1923 *Phil. Trans. R. Soc.* **223**, 289.

TSAMERET, A. & STEINBERG, V. 1991 *Phys. Rev. Lett.* **67**, 3392.

THUAL, O. & FAUVE, S. 1988 *J. Phys. (Paris)* **49**, 1829.

WALDEN, R. W., KOLODNER, P., PASSNER, A. & SURKO, C. M. 1985 *Phys. Rev. Lett.* **55**, 496.

WESFREID, J. E., BRAND, H. R., MANNEVILLE, P., ALBINET, G. & BOCCARA, N. (ed.) 1988 *Propagation in Systems Far from Equilibrium.* Springer.

ZAĬTSEV, V. M. & SHLIOMIS, M. I. 1970 *Zh. Exsp. Teor. Fiz.* **59**, 1583 [1971 *Sov. Phys. JETP* **32**, 866].